Signal Processing and Propagation for Aeroacoustic Sensor Networks

Richard J. Kozick*, Brian M. Sadler†, and D. Keith Wilson‡

*Bucknell University
Dept. of Electrical Engineering, Lewisburg, PA 17837, USA
Tel: 570-577-1129, Fax: 570-577-1822, e-mail: `kozick@bucknell.edu`

†Army Research Laboratory
AMSRL-CI-CN, 2800 Powder Mill Road, Adelphi, MD 20783, USA
Tel: 301-394-1239, Fax: 301-394-1197, e-mail: `bsadler@arl.army.mil`

‡ U.S. Army Cold Regions Research and Engineering Laboratory
CEERD-RC, 72 Lyme Road, Hanover, NH 03755-1290, USA
Tel: 603-646-4764, Fax: 603-646-4640 e-mail: `d.keith.wilson@erdc.usace.army.mil`

Chapter for *Frontiers in Distributed Sensor Networks*,
S.S. Iyengar and R.R. Brooks (Eds.), CRC Press

Submitted on July 23, 2003

Contents

1 Introduction 1

2 Models for Source Signals and Propagation 3

- 2.1 Basic considerations 4
- 2.2 Narrowband model with no scattering 7
- 2.3 Narrowband model with scattering 10
- 2.4 Model for extinction coefficients 14
- 2.5 Multiple frequencies and sources 16

3 Signal Processing 18

- 3.1 Angle of arrival estimation 18
  - 3.1.1 Narrowband AOA estimation with scattering 18
  - 3.1.2 Wideband AOA estimation without scattering 19
  - 3.1.3 Performance analysis and wideband beamforming 22
  - 3.1.4 AOA experiments 22
- 3.2 Localization with distributed sensor arrays 24
  - 3.2.1 Model for array of arrays 26
  - 3.2.2 Cramér-Rao bounds (CRBs) and examples 28
  - 3.2.3 TDE and examples 31
- 3.3 Tracking moving sources 34
- 3.4 Detection and classification 36

4 Concluding Remarks 38

1 Introduction

Passive sensing of acoustic sources is attractive in many respects, including the relatively low signal bandwidth of sound waves, the loudness of most sources of interest, and the inherent difficulty of disguising or concealing emitted acoustic signals. The availability of inexpensive, low-power sensing and signal processing hardware enables application of sophisticated real-time signal processing. Among the many applications of aeroacoustic sensors, we focus in this chapter on detection and localization of ground and air (both jet and rotary) vehicles from ground-based sensor networks. Tracking and classification are briefly considered as well.

Elaborate, aeroacoustic systems for passive vehicle detection were developed as early as World War I [1]. Despite this early start, interest in aeroacoustic sensing has generally lagged other technologies until the recent packaging of small microphones, digital signal processing, and wireless communications into compact, unattended systems. An overview of modern outdoor acoustic sensing is presented by Becker and Güdesen [2]. Experiments in the early 1990's, such as those described by Srour and Robertson [3], demonstrated the feasibility of network detection, array processing, localization, and multiple target tracking via Kalman filtering. Many of the fundmental issues and challenges described by Srour and Robertson remain relevant today.

Except at very close range, the typical operating frequency range we consider is roughly 30 to 250 Hz. Below 30 Hz (the infrasonic regime), wavelengths are greater than 10 m so that rather large arrays may be required. Furthermore, wind noise (random pressure fluctuations induced by atmospheric turbulence) reduces the observed signal-to-noise ratio (SNR) [2]. At frequencies above several hundred Hz, molecular absorption of sound and interference between direct and ground-reflected waves attenuate received signals significantly [4]. In effect, the propagation environment acts as a low pass filter; this is particularly evident at longer ranges.

Aeroacoustics is inherently an ultra-wideband array processing problem, e.g., operating in $[30, 250]$ Hz yields a 157% fractional bandwidth centered at 140 Hz. To process under the narrow band array assumptions will require the fractional bandwidth to be on the order of a few percent or less, limiting the bandwidth to perhaps a few Hz in this example. The wide bandwidth significantly complicates the array signal processing, including angle-of-arrival (AOA) estimation, wideband Doppler compensation, beamforming, and blind source separation (which becomes convolutional).

The typical source of interest here has a primary contribution due to rotating machinery (engines), and may include tire and/or exhaust noise, vibrating surfaces, and other contributions.

Internal combustion engines typically exhibit a strong sum of harmonics acoustic signature tied to the cylinder firing rate, a feature that can be exploited in virtually all phases of signal processing. Tracked vehicles also exhibit tread slap, which can produce very strong spectral lines, while helicopters produce strong harmonic sets related to the blade rotation rates. Turbine engines, on the other hand, exhibit a much more smoothly broad spectrum and consequently call for different algorithmic approaches in some cases. Many heavy vehicles and aircraft are quite loud and can be detected from ranges of several km or more. Ground vehicles may also produce significant seismic waves, although we do not consider multi-modal sensing or sensor fusion here.

The problem is also complicated by time-varying factors that are difficult to model, such as source signature variations resulting from acceleration/deceleration of vehicles, changing meteorological conditions, multiple soft and loud sources, aspect angle source signature dependency, Doppler shifts (with 1-Hz shifts at a 100-Hz center frequency not unusual), multipath, and so on. Fortunately, at least for many sources of interest, a piecewise stationary model is reasonable on time scales of one second or less, although fast moving sources may require some form of time-varying model.

Sensor networks of interest are generally connected with wireless links, and are battery powered. Consequently, the node power budget may be dominated by the communications (radio). Therefore, a fundamental design question is how to perform distributed processing in order to reduce communication bandwidth, while achieving near optimal detection, estimation, and classification performance. We focus on this question, taking the aeroacoustic environment into account.

In particular, we consider the impact of random atmospheric inhomogeneities (primarily thermal and wind variations caused by turbulence) on the ability of an aeroacoustic sensor network to localize sources. Given that turbulence induces acoustical index-of-refraction variations several orders of magnitude greater than corresponding electromagnetic variations [5], this impact is quite significant. Turbulent scattering of sound waves causes random fluctuations in signals as observed at a single sensor, with variations occurring on time scales from roughly one to hundreds of seconds in our frequency range of interest [6, 7, 8]. Scattering is also responsible for losses in the observed spatial coherence measured between two sensors [9, 10, 11]. The scattering may be weak or strong, which are analogous to Rician and Rayleigh fading in radio propagation, respectively.

The impact of spatial coherence loss is significant, and generally becomes worse with increasing distance between sensors. This effect, as well as practical size constraints, limits individual sensor node array apertures to perhaps a few meters. At the same time, the acoustic wavelengths λ of interest are about 1 to 10 m ($\lambda = (330 \text{ m/s})/(30 \text{ Hz}) = 11$ m at 30 Hz, and $\lambda = 1.32$ m at 250 Hz). Thus, the typical array aperture will only span a fraction of a wavelength, and accurate AOA estimation requires wideband superresolution methods. The source may generally be considered to be in the far field of these small arrays. Indeed, if it is in the near field, then the rate of change of the AOA as the source moves past the array must be considered.

The signal-coherence characteristics suggest deployment of multiple, small-baseline arrays as nodes within an overall large-baseline array (see Figure 7 in Section 3.2). The source is intended to be in the near-field of the large-baseline array. Exploitation of this larger baseline is highly desirable, as it potentially leads to very accurate localization. We characterize this problem in terms of the atmosphere-induced spatial coherence loss, and show fundamental bounds on the ability to localize a source in such conditions. This leads to a family of localization approaches, spanning triangulation (which minimizes inter-node communication), to time-delay estimation, to fully centralized processing (which maximizes communication use and is therefore undesirable). The achievable localization accuracy depends on both the propagation conditions and the time-bandwidth product of the source.

The chapter is organized as follows. In Section 2 we introduce the wideband source array signal processing model, develop the atmospheric scattering model, and incorporate the scattering into the array model. We consider array signal processing in Section 3, including narrowband AOA estimation with scattering present. We review wideband AOA estimation techniques, and highlight various aeroacoustic wideband AOA experiments. Next, we consider localization with multiple nodes (arrays) in the presence of scattering. We develop fundamental and tight performance bounds on time delay estimation in the turbulent atmosphere, as well as bounds on localization. Localization performance is illustrated via simulation and experiments. We then briefly consider the propagation impact on detection and classification. Finally, in Section 4 we consider some emerging aspects and open questions.

2 Models for Source Signals and Propagation

In this section, we present a general model for the signals received by an aeroacoustic sensor array. We begin by briefly considering models for the signals emitted by ground vehicles and aircraft in Section 2.1. Atmospheric phenomena affecting propagation of the signal are also summarized. In Section 2.2, we consider the simplest possible case for the received signals: a single nonmoving source emits a sinusoidal waveform, and the atmosphere induces no scattering (randomization of the signal). Then in Section 2.3, we extend the model to include the effects of scattering, and in Section 2.4, approximate models for the scattering as a function of source range, frequency, and atmospheric conditions are presented. The model is extended to multiple sources and multiple frequencies (wideband) in Section 2.5.

2.1 Basic considerations

As we noted in the Introduction, the sources of interest typically have spectra that are harmonic lines, or have relatively continuous broadband spectra, or some combination. The signal processing for detection, localization, and classification is highly dependent on whether the source spectrum is harmonic or broadband. For example, broadband sources allow time-difference of arrival processing for localization, while harmonic sources allow differential Doppler estimation.

Various deterministic and random source models may be employed. Autoregressive (AR) processes are well suited to modeling sums of harmonics, at least for the case of a single source, and may be used for detection, Doppler estimation, filtering, AOA estimation, and so on [12, 13, 14]. Sum of harmonic models, with unknown harmonic structure, lead naturally to detection tests in the frequency domain [15].

More generally, a Gaussian random process model may be employed to describe both harmonic sets and wideband sources [16]; we adopt such a point of view here. We also assume a piecewise stationary (quasi-static) viewpoint: although the source may actually be moving, the processing interval is assumed to be short enough that the signal characteristics are nearly constant.

Four phenomena are primarily responsible for modifying the source signal to produce the actual signal observed at the sensor array:

1. The propagation delay from the source to the sensors.
2. Random fluctuations in the amplitude and phase of the signals caused by scattering from random inhomogeneities in the atmosphere such as turbulence.
3. Additive noise at the sensors caused by thermal noise, wind noise, and directional interference.
4. Transmission loss caused by spreading of the wavefronts, refraction by wind and temperature gradients, ground interactions, and molecular absorption of sound energy.

Thermal noise at the sensors is typically independent from sensor to sensor. In contrast, interference from an undesired source produces additive noise that is (spatially) correlated from sensor to sensor. Wind noise, which consists of low-frequency turbulent pressure fluctuations intrinsic to the atmospheric flow (and, to a lesser extent, flow distortions induced by the microphone itself [17, 2]), exhibits high spatial correlation over distances of several meters [18].

The transmission loss (TL) is defined as the diminishment in sound energy from a reference value S_{ref}, which would hypothetically be observed in free space at 1 m from the source, to the actual value observed at the sensor S. To a first approximation, the sound energy spreads spherically; that is, it diminishes as the inverse of the squared distance from the source. In actuality the TL for sound wave propagating near the ground involves many complex, interacting phenomena, so that the spherical spreading condition is rarely observed in practice, except perhaps within the first 10 to 30 m [4]. Fortunately, several well refined and accurate numerical procedures for calculating TL have been developed [19]. For simplicity, here we model S as a deterministic parameter, which is reasonable when the state of the atmosphere does not change dramatically during the data collection.

Particularly significant to the present discussion is the second phenomenon in the preceding list, namely scattering by turbulence. The turbulence consists of random atmospheric motions occurring on time scales from seconds to several minutes. Scattering from these motions causes random fluctuations in the complex signals at the individual sensors and diminishes the cross coherence of signals between sensors. The effects of scattering on array performance will be analyzed in Sections 2.2 and 2.4.

The sinusoidal source signal that is measured at the reference distance of 1 m from the source is written

$$s_{\text{ref}}(t) = \sqrt{S_{\text{ref}}} \cos(2\pi f_o t + \chi), \tag{1}$$

where the frequency of the tone is $f_o = \omega_o/(2\pi)$ Hz, the period is T_o sec, the phase is χ, and the amplitude is $\sqrt{S_{\text{ref}}}$. The sound waves propagate with wavelength $\lambda = c/f_o$, where c is the speed of sound. The wavenumber is $k = 2\pi/\lambda = \omega_o/c$. We will represent sinusoidal and narrowband signals by their complex envelope, which may be defined in two ways, as in (2):

$$\begin{aligned} \mathcal{C}\{s_{\text{ref}}(t)\} = \widetilde{s}_{\text{ref}}(t) = s_{\text{ref}}^{(\text{I})}(t) + j\, s_{\text{ref}}^{(\text{Q})}(t) &= [s_{\text{ref}}(t) + j\,\mathcal{H}\{s_{\text{ref}}(t)\}] \exp(-j2\pi f_o t) \qquad (2)\\ &= \sqrt{S_{\text{ref}}} \exp(j\chi). \qquad (3) \end{aligned}$$

We will represent the complex envelope of a quantity with the notation $\mathcal{C}\{\cdot\}$ or $\widetilde{(\cdot)}$, the in-phase component with $(\cdot)^{(\text{I})}$, the quadrature component with $(\cdot)^{(\text{Q})}$, and the Hilbert transform with $\mathcal{H}\{\cdot\}$. The in-phase (I) and quadrature (Q) components of a signal are obtained by the processing in Figure 2. The FFT is often used to approximate the processing in Figure 2 for a finite block of data, where the real and imaginary parts of the FFT coefficient at frequency f_o are proportional to the I and Q components, respectively. The complex envelope of the sinusoid in (1) is given by (3), which is not time-varying, so the average power is $|\widetilde{s}_{\text{ref}}(t)|^2 = S_{\text{ref}}$.

It is easy to see for the sinusoidal signal (1) that shifting $s_{\text{ref}}(t)$ in time causes a phase shift in the corresponding complex envelope, i.e., $\mathcal{C}\{s_{\text{ref}}(t-\tau_o)\} = \exp(-j2\pi f_o \tau_o)\, \widetilde{s}_{\text{ref}}(t)$. A similar property is true for *narrowband* signals whose frequency spectrum is confined to a bandwidth B Hz around a center frequency f_o Hz, where $B \ll f_o$. For a narrowband signal $z(t)$ with complex envelope $\widetilde{z}(t)$, a shift in time is well-approximated by a phase shift in the corresponding complex envelope,

$$\mathcal{C}\{z(t-\tau_o)\} \approx \exp(-j2\pi f_o \tau_o)\, \widetilde{z}(t) \quad \text{(narrowband approximation).} \tag{4}$$

Equation (4) is the well-known Fourier transform relationship between shifts in time and phase shifts that are linearly proportional to frequency. The approximation is accurate when the frequency band is narrow enough so that the linearly increasing phase shift is close to $\exp(-j2\pi f_o \tau_o)$ over the band.

The source and array geometry is illustrated in Figure 1. The source is located at coordinates (x_s, y_s) in the (x, y) plane. The array contains N sensors, with sensor n located at $(x_o + \Delta x_n, y_o + \Delta y_n)$, where (x_o, y_o) is the center of the array and $(\Delta x_n, \Delta y_n)$ is the relative sensor location. The propagation time from the source to the array center is

$$\tau_o = \frac{d_o}{c} = \frac{1}{c}\left[(x_s - x_o)^2 + (y_s - y_o)^2\right]^{1/2}, \tag{5}$$

where d_o is the distance from the source to the array center. The propagation time from the source to sensor n is

$$\tau_n = \frac{d_n}{c} = \frac{1}{c}\left[(x_s - x_o - \Delta x_n)^2 + (y_s - y_o - \Delta y_n)^2\right]^{1/2}. \tag{6}$$

Let us denote the array diameter by $L = \max\{\rho_{mn}\}$, where ρ_{mn} is the separation between sensors m and n, as shown in Figure 1. The source is in the *far-field* of the array when the source distance satisfies $d_o \gg L^2/\lambda$, in which case (6) may be approximated with the first term in the Taylor series $(1+u)^{1/2} \approx 1 + u/2$. Then $\tau_n \approx \tau_o + \tau_{o,n}$ with error that is much smaller than the source period, T_o, where

$$\tau_{o,n} = -\frac{1}{c}\left[\frac{x_s - x_o}{d_o}\Delta x_n + \frac{y_s - y_o}{d_o}\Delta y_n\right] = -\frac{1}{c}\left[(\cos\phi)\Delta x_n + (\sin\phi)\Delta y_n\right]. \tag{7}$$

The angle ϕ is the azimuth bearing, or angle of arrival (AOA), as shown in Figure 1. In the far-field, the spherical wavefront is approximated as a plane wave over the array aperture, so the bearing ϕ contains the available information about the source location. For array diameters $L < 2$ m and tone frequencies $f_o < 200$ Hz so that $\lambda > 1.5$ m, the quantity $L^2/\lambda < 2.7$ m. Thus the far-field is valid for source distances on the order of 10's of meters. For smaller source distances and/or larger array apertures, the curvature of the wavefront over the array aperture must be included in τ_n according to (6). We develop the model for the far-field case in the next section. However, the extension to the near-field is easily accomplished by redefining the array response vector ($\mathbf{a}$ in (20)) to include the wavefront curvature with $a_n = \exp(-j2\pi f_o \tau_n)$.

2.2 Narrowband model with no scattering

Here we present the model for the signals impinging on the sensor array when there is no scattering. Using the far-field approximation, the noisy measurements at the sensors are

$$z_n(t) = s_n\left(t - \tau_o - \tau_{o,n}\right) \; + \; w_n(t), \quad n = 1, \ldots, N. \tag{8}$$

In the absence of scattering, the signal components are pure sinusoids,

$$s_n(t) = \sqrt{S}\, \cos\left(2\pi f_o t + \chi\right). \tag{9}$$

The $w_n(t)$ are additive, white, Gaussian noise (AWGN) processes that are real-valued, continuous-time, zero-mean, jointly wide-sense stationary, and mutually uncorrelated at distinct sensors with power spectral density (PSD) $(\mathcal{N}_o/2)$ W/Hz. That is, the noise correlation properties are

$$\begin{aligned} E\{w_n(t)\} &= 0, \quad -\infty < t < \infty, \; n = 1, \ldots, N & (10) \\ r_{w,mn}(\xi) = E\{w_m(t+\xi) w_n(t)\} &= r_w(\xi)\, \delta_{mn}, & (11) \end{aligned}$$

where $E\{\cdot\}$ denotes expectation and $r_w(\xi) = (\mathcal{N}_o/2)\, \delta(\xi)$ is the noise autocorrelation function that is common at all sensors. The Dirac delta function is $\delta(\cdot)$, and the Kronecker delta function is $\delta_{mn} = 1$ if $m = n$ and 0 otherwise. As noted above, modeling the noise as spatially white may be inaccurate if wind noise or interfering sources are present in the environment. The noise PSD is

$$G_w(f) = \mathcal{F}\{r_w(\xi)\} = \frac{\mathcal{N}_o}{2}, \tag{12}$$

where $\mathcal{F}\{\cdot\}$ denotes Fourier transform. With no scattering, the complex envelope of $z_n(t)$ in (8) and (9) is, using (4),

$$\begin{aligned} \widetilde{z}_n(t) &= \exp\left[-j\; (\omega_o \tau_o + \omega_o \tau_{o,n})\right]\, \widetilde{s}_n(t) \; + \; \widetilde{w}_n(t) \\ &= \sqrt{S}\, \exp\left[j\; (\chi - \omega_o \tau_o)\right]\, \exp\left[-j\, \omega_o \tau_{o,n}\right] \; + \; \widetilde{w}_n(t), \end{aligned} \tag{13}$$

where the complex envelope of the narrowband source component is

$$\widetilde{s}_n(t) = \sqrt{S}\, e^{j\chi}, \quad n = 1, \dots, N \quad \text{(no scattering)}. \tag{14}$$

We assume that the complex envelope is lowpass filtered with bandwidth from $[-B/2, B/2]$ Hz, e.g., as in Figure 2. Assuming that the lowpass filter is ideal, the complex envelope of the noise, $\widetilde{w}_n(t)$, has PSD and correlation

$$\begin{aligned}
G_{\tilde{w}}(f) &= (2\mathcal{N}_o)\,\text{rect}\left(\frac{f}{B}\right) && (15)\\
r_{\tilde{w}}(\xi) &= E\{\widetilde{w}_n(t+\xi)\widetilde{w}_n(t)^*\} = \mathcal{F}^{-1}\left\{G_{\tilde{w}}(f)\right\} = (2\mathcal{N}_o B)\,\text{sinc}\,(B\xi) && (16)\\
r_{\tilde{w},mn}(\xi) &= E\{\widetilde{w}_m(t+\xi)\widetilde{w}_n(t)^*\} = r_{\tilde{w}}(\xi)\,\delta_{mn}, && (17)
\end{aligned}$$

where $(\cdot)^*$ denotes complex conjugate, $\text{rect}(u) = 1$ for $-1/2 < u < 1/2$ and 0 otherwise, and $\text{sinc}(u) = \sin(\pi u)/(\pi u)$. Note that the noise samples are uncorrelated (and independent since Gaussian) at sample times spaced by $1/B$ sec. In practice, the noise PSD $G_{\tilde{w}}(f)$ is neither flat nor perfectly band-limited as in (15). However, the lowpass filtering to bandwidth B Hz implies that the noise samples have decreasing correlation for time spacing greater than $1/B$ sec.

Let us define the vectors

$$\widetilde{\mathbf{z}}(t) = \begin{bmatrix} \widetilde{z}_1(t) \\ \vdots \\ \widetilde{z}_N(t) \end{bmatrix}, \quad \widetilde{\mathbf{s}}(t) = \begin{bmatrix} \widetilde{s}_1(t) \\ \vdots \\ \widetilde{s}_N(t) \end{bmatrix}, \quad \widetilde{\mathbf{w}}(t) = \begin{bmatrix} \widetilde{w}_1(t) \\ \vdots \\ \widetilde{w}_N(t) \end{bmatrix}. \tag{18}$$

Then using (13) with (7),

$$\widetilde{\mathbf{z}}(t) = \sqrt{S}\,\exp\left[j\ (\chi - \omega_o \tau_o)\right]\mathbf{a} \ + \ \widetilde{\mathbf{w}}(t) = \sqrt{S}\, e^{j\theta}\,\mathbf{a} \ + \ \widetilde{\mathbf{w}}(t), \tag{19}$$

where $\mathbf{a}$ is the array steering vector (or array manifold)

$$\mathbf{a} = \begin{bmatrix} \exp\left[j\,k\ ((\cos\phi)\Delta x_1 + (\sin\phi)\Delta y_1)\right] \\ \vdots \\ \exp\left[j\,k\ ((\cos\phi)\Delta x_N + (\sin\phi)\Delta y_N)\right] \end{bmatrix} \tag{20}$$

with $k = \omega_o/c$. Note that the steering vector, $\mathbf{a}$, depends on the frequency ω_o, the sensor locations $(\Delta x_n, \Delta y_n)$, and the source bearing ϕ. The common phase factor at all of the sensors, $\exp\left[j\ (\chi - \omega_o\tau_o)\right] = \exp\left[j\ (\chi - kd_o)\right]$, depends on the phase of the signal emitted by the source (χ) and the propagation distance to the center of the array (kd_o). We simplify the notation and define

$$\theta \overset{\triangle}{=} \chi - kd_o, \tag{21}$$

which is a deterministic parameter.

In preparation for the introduction of scattering into the model, let us write expressions for the first- and second-order moments of the vectors $\widetilde{\mathbf{s}}(t)$ and $\widetilde{\mathbf{z}}(t)$. Let $\mathbf{1}$ be an $N \times 1$ vector of 1's, $\mathbf{R}_{\tilde{\mathbf{z}}}(\xi) = E\{\widetilde{\mathbf{z}}(t+\xi)\,\widetilde{\mathbf{z}}(t)^\dagger\}$ be the $N \times N$ cross-correlation function matrix with (m,n) element $r_{\tilde{z},mn}(\xi) = E\{\widetilde{z}_m(t+\xi)\widetilde{z}_n(t)^*\}$, and $\mathbf{G}_{\tilde{\mathbf{z}}}(f) = \mathcal{F}\{\mathbf{R}_{\tilde{\mathbf{z}}}(\xi)\}$ be the cross-spectral density (CSD) matrix, then

$$E\{\widetilde{\mathbf{s}}(t)\} = \sqrt{S}\,e^{j\chi}\,\mathbf{1} \qquad\qquad E\{\widetilde{\mathbf{z}}(t)\} = \sqrt{S}\,e^{j\theta}\,\mathbf{a} \tag{22}$$

$$\mathbf{R}_{\tilde{\mathbf{s}}}(\xi) = S\,\mathbf{1}\mathbf{1}^T \qquad\qquad \mathbf{R}_{\tilde{\mathbf{z}}}(\xi) = S\,\mathbf{a}\mathbf{a}^\dagger \;+\; r_{\tilde{w}}(\xi)\,\mathbf{I} \tag{23}$$

$$\mathbf{G}_{\tilde{\mathbf{s}}}(f) = S\,\mathbf{1}\mathbf{1}^T\,\delta(f) \qquad\qquad \mathbf{G}_{\tilde{\mathbf{z}}}(f) = S\,\mathbf{a}\mathbf{a}^\dagger\,\delta(f) \;+\; G_{\tilde{w}}(f)\,\mathbf{I} \tag{24}$$

$$E\{\widetilde{\mathbf{s}}(t)\widetilde{\mathbf{s}}(t)^\dagger\} = \mathbf{R}_{\tilde{\mathbf{s}}}(0) = S\,\mathbf{1}\mathbf{1}^T \qquad\qquad E\{\widetilde{\mathbf{z}}(t)\widetilde{\mathbf{z}}(t)^\dagger\} = \mathbf{R}_{\tilde{\mathbf{z}}}(0) = S\,\mathbf{a}\mathbf{a}^\dagger \;+\; \sigma_{\tilde{w}}^2\,\mathbf{I}, \tag{25}$$

where $(\cdot)^T$ denotes transpose, $(\cdot)^*$ denotes complex conjugate, $(\cdot)^\dagger$ denotes complex conjugate transpose, $\mathbf{I}$ is the $N \times N$ identity matrix, and $\sigma_{\tilde{w}}^2$ is the variance of the noise samples,

$$\sigma_{\tilde{w}}^2 = E\left\{|\widetilde{\mathbf{w}}(t)|^2\right\} = r_{\tilde{w}}(0) = 2\mathcal{N}_o B. \tag{26}$$

Note from (24) that the PSD at each sensor contains a spectral line since the source signal is sinusoidal. Note from (25) that at each sensor, the average power of the signal component is S, so the signal to noise ratio (SNR) at each sensor is

$$\text{SNR} = \frac{S}{\sigma_{\tilde{w}}^2} = \frac{S}{2\mathcal{N}_o B}. \tag{27}$$

The complex envelope vector $\widetilde{\mathbf{z}}(t)$ is typically sampled at a rate $f_s = B$ samples/sec, so the samples are spaced by $T_s = 1/f_s = 1/B$ sec,

$$\widetilde{\mathbf{z}}(iT_s) = \sqrt{S}\,e^{j\theta}\,\mathbf{a} \;+\; \widetilde{\mathbf{w}}(iT_s), \quad i = 0, \ldots, T-1. \tag{28}$$

According to (17), the noise samples are spatially independent as well as temporally independent, since $r_{\tilde{w}}(iT_s) = r_{\tilde{w}}(i/B) = 0$. Thus the vectors $\widetilde{\mathbf{z}}(0), \widetilde{\mathbf{z}}(T_s), \ldots, \widetilde{\mathbf{z}}((T-1)T_s)$ in (28) are independent and identically distributed (iid) with complex normal distribution, which we denote by $\widetilde{\mathbf{z}}(iT_s) \sim \text{CN}\left(\mathbf{m}_{\tilde{\mathbf{z}}}, \mathbf{C}_{\tilde{\mathbf{z}}}\right)$, with mean and covariance matrix

$$\mathbf{m}_{\tilde{\mathbf{z}}} = \sqrt{S}\,e^{j\theta}\,\mathbf{a} \;\text{ and }\; \mathbf{C}_{\tilde{\mathbf{z}}} = \sigma_{\tilde{w}}^2\,\mathbf{I} \quad \text{(no scattering).} \tag{29}$$

The joint probability density function for $\text{CN}\left(\mathbf{m}_{\tilde{\mathbf{z}}}, \mathbf{C}_{\tilde{\mathbf{z}}}\right)$ is given by [20]

$$f\left(\widetilde{\mathbf{z}}\right) = \frac{1}{\pi^N \det\left(\mathbf{C}_{\tilde{\mathbf{z}}}\right)} \exp\left[-\left(\widetilde{\mathbf{z}} - \mathbf{m}_{\tilde{\mathbf{z}}}\right)^\dagger\,\mathbf{C}_{\tilde{\mathbf{z}}}^{-1}\,\left(\widetilde{\mathbf{z}} - \mathbf{m}_{\tilde{\mathbf{z}}}\right)\right], \tag{30}$$

where "det" denotes determinant. In the absence of scattering, the information about the source location (bearing) is contained in the mean of the sensor observations. If the T time samples in (28) are coherently averaged, then the resulting SNR per sensor is T times that in (27), so $\text{SNR}' = T \cdot (S/\sigma_{\tilde{w}}^2) = T \cdot [S/(2\mathcal{N}_o/T_s)] = \mathcal{T} \cdot S/(2\mathcal{N}_o)$, where $\mathcal{T} = T \cdot T_s$ is the total observation time, in seconds.

2.3 Narrowband model with scattering

Next, we include the effects of scattering by atmospheric turbulence in the model for the signals measured at the sensors in the array. As mentioned earlier, the scattering introduces random fluctuations in the signals and diminishes the cross coherence between the array elements. The formulation we present for the scattering effects was developed by Wilson, Collier and others [21, 22, 23, 11, 24, 25, 26]. The reader may refer to these studies for details about the physical modeling and references to additional primary source material. Several assumptions and simplifications are involved in the formulation: (1) the propagation is line-of-sight (no multipath), (2) the additive noise is independent from sensor to sensor, and (3) the random fluctuations caused by scattering are complex, circular, Gaussian random processes with partial correlation between the sensors.

The line-of-sight propagation assumption is consistent with Section 2.2 and is reasonable for propagation over fairly flat, open terrain in the frequency range of interest here (below several hundred Hz). Significant acoustic multipath may result from reflections off hard objects such as buildings, trees, and (sometimes) the ground. Multipath can also result from refraction of sound waves by vertical gradients in the wind and temperature.

By assuming independent, additive noise, we ignore the potential spatial correlation of wind noise and interference from other undesired sources. This restriction may be averted by extending the models to include spatially-correlated additive noise, although the signal processing may be more complicated in this case.

Modeling of the scattered signals as complex, circular, Gaussian random processes is a substantial improvement on the constant signal model (Section 2.2), but it is, nonetheless, rather idealized. Waves that have propagated through a random medium can exhibit a variety of statistical behaviors, depending on such factors as the strength of the turbulence, the propagation distance, and the ratio of the wavelength to the predominant eddy size [27, 5]. Experimental studies [28, 29, 8] conducted over short horizontal propagation distances with frequencies below 1000 Hz demonstrate that the effect of turbulence is highly significant, with phase variations much larger than 2π rad and deep fades in amplitude often developing. The measurements demonstrate that the Gaussian model is valid in many conditions, although non-Gaussian scattering characterized by large phase but small amplitude variations is observed at some frequencies and propagation distances. The Gaussian model applies in many cases of interest, and we apply it in this chapter. The effect of non-Gaussian signal scattering on aeroacoustic array performance remains to be determined.

The scattering modifies the complex envelope of the signals at the array by spreading a portion of the power from the (deterministic) mean component into a zero-mean random process with a PSD centered at 0 Hz. We assume that the bandwidth of the scattered signal, which we denote by B, is much smaller than the tone frequency, f_o. The *saturation* parameter [26, 25], denoted by $\Omega \in [0, 1]$, defines the fraction of average signal power that is scattered from the mean into the random component. The scattering may be *weak* ($\Omega \approx 0$) or *strong* ($\Omega \approx 1$), which are analogous to Rician and Rayleigh fading in the radio propagation literature. The modification of (8), (9), (13), and (14) to include scattering is as follows, where $\widetilde{z}_n(t)$ is the signal measured at sensor n:

$$\widetilde{z}_n(t) = \exp\left[-j \ (\omega_o \tau_o + \omega_o \tau_{o,n})\right] \widetilde{s}_n(t) \ + \ \widetilde{w}_n(t) \tag{31}$$

$$\widetilde{s}_n(t) = \sqrt{(1-\Omega)S}\, e^{j\chi} \ + \ \widetilde{v}_n(t)\, e^{j\chi}, \ \ n = 1, \ldots, N \text{ (with scattering).} \tag{32}$$

In order to satisfy conservation of energy with $E\{|\widetilde{s}_n(t)|^2\} = S$, the average power of the scattered component must be $E\{|\widetilde{v}_n(t)|^2\} = \Omega\, S$. The value of the saturation Ω and the correlation properties of the vector of scattered processes, $\widetilde{\mathbf{v}}(t) = [\widetilde{v}_1(t), \ldots, \widetilde{v}_N(t)]^T$, depend on the source distance (d_o) and the meteorological conditions. The vector of scattered processes $\widetilde{\mathbf{v}}(t)$ and the additive noise vector $\widetilde{\mathbf{w}}(t)$ contain zero-mean, jointly wide-sense stationary, complex, circular Gaussian random processes. The scattered processes and the noise are modeled as independent, $E\{\widetilde{\mathbf{v}}(t+\xi)\widetilde{\mathbf{w}}(t)^\dagger\} = \mathbf{0}$. The noise is described by (15)-(17), while the saturation Ω and statistics of $\widetilde{\mathbf{v}}(t)$ are determined by the "extinction coefficients" of the first and second moments of $\widetilde{\mathbf{s}}(t)$. As will be discussed in Section 2.4, approximate analytical models for the extinction coefficients are available from physical modeling of the turbulence in the atmosphere. In the remainder of this section, we define the extinction coefficients and relate them to Ω and the statistics of $\widetilde{\mathbf{v}}(t)$, thereby providing models for the sensor array data that include turbulent scattering by the atmosphere.

We denote the extinction coefficients for the first and second moments of $\widetilde{\mathbf{s}}(t)$ by μ and $\nu(\rho_{mn})$, respectively, where ρ_{mn} is the distance between sensors m and n (see Figure 1). The extinction coefficients are implicitly defined as follows:

$$E\{\widetilde{s}_n(t)\} = \sqrt{(1-\Omega)S}\, e^{j\chi} \qquad \triangleq \sqrt{S}\, e^{j\chi}\, e^{-\mu d_o} \tag{33}$$

$$r_{\tilde{s},mn}(0) = E\{\widetilde{s}_m(t)\widetilde{s}_n(t)^*\} = (1-\Omega)S \ + \ r_{\tilde{v},mn}(0) \qquad \triangleq S\, e^{-\nu(\rho_{mn}) d_o} \tag{34}$$

where

$$r_{\tilde{s},mn}(\xi) = E\{\widetilde{s}_m(t+\xi)\widetilde{s}_n(t)^*\} = (1-\Omega)S \ + \ r_{\tilde{v},mn}(\xi). \tag{35}$$

The right sides of (33) and (34) are the first and second moments *without* scattering, from (22) and (23), respectively, multiplied by a factor that decays exponentially with increasing distance d_o from the source. From (33), we obtain

$$\sqrt{(1-\Omega)} = e^{-\mu d_o} \ \text{ and } \ \Omega = 1 - e^{-2\mu d_o}. \tag{36}$$

Also, by conservation of energy with $m = n$ in (34), adding the average powers in the unscattered and scattered components of $\widetilde{s}_n(t)$ must equal S, so

$$r_{\tilde{s}}(0) = E\left\{|\widetilde{s}_n(t)|\right\} = e^{-2\mu d_o}S \ + \ r_{\tilde{v}}(0) = S \tag{37}$$

$$\Longrightarrow r_{\tilde{v}}(0) = E\left\{|\widetilde{v}_n(t)|\right\} = \int_{-\infty}^{\infty} G_{\tilde{v}}(f)\,df = \left(1 - e^{-2\mu d_o}\right) S = \Omega\, S, \tag{38}$$

where $r_{\tilde{v}}(\xi) = E\{\widetilde{v}_n(t+\xi)\widetilde{v}_n(t)^*\}$ is the autocorrelation function (which is the same for all n) and $G_{\tilde{v}}(f)$ is the corresponding PSD. Therefore for source distances $d_o \ll 1/(2\mu)$, the saturation $\Omega \approx 0$ and most of the energy from the source arrives at the sensor in the unscattered (deterministic mean) component of $\widetilde{s}_n(t)$. For source distances $d_o \gg 1/(2\mu)$, the saturation $\Omega \approx 1$ and most of the energy arrives in the scattered (random) component.

Next, we use (34) to relate the correlation of the scattered signals at sensors m and n, $r_{\tilde{v},mn}(\xi)$, to the second moment extinction coefficient, $\nu(\rho_{mn})$. Since the autocorrelation of $\widetilde{v}_n(t)$ is identical at each sensor n and equal to $r_{\tilde{v}}(\xi)$, and assuming that the PSD $G_{\tilde{v}}(f)$ occupies a narrow bandwidth centered at 0 Hz, the cross-correlation and cross-spectral density satisfy

$$r_{\tilde{v},mn}(\xi) = \gamma_{mn}\, r_{\tilde{v}}(\xi) \ \text{ and } \ G_{\tilde{v},mn}(f) = \mathcal{F}\{r_{\tilde{v},mn}(\xi)\} = \gamma_{mn} G_{\tilde{v}}(f), \tag{39}$$

where $|\gamma_{mn}| \leq 1$ is a measure of the coherence between $\widetilde{v}_m(t)$ and $\widetilde{v}_n(t)$. The definition of γ_{mn} as a *constant* includes an approximation that the coherence does not vary with frequency, which is reasonable when the bandwidth of $G_{\tilde{v}}(f)$ is narrow. Although systematic studies of the coherence time of narrowband acoustic signals have not been made, data and theoretical considerations (such as in [27, Sec. 8.4]) are consistent with values ranging from tens of seconds to several minutes in the frequency range $[50, 250]$ Hz. Therefore the bandwidth of $G_{\tilde{v}}(f)$ may be expected to be less than 1 Hz. The bandwidth B in the lowpass filters for the complex amplitude in Figure 2 should be chosen to be equal to the bandwidth of $G_{\tilde{v}}(f)$. We assume that γ_{mn} in (39) is real-valued and non-negative, which implies that phase fluctuations at sensor pairs are not biased toward positive or negative values. Then using (39) with (38) and (36) in (34) yields the following relation between γ_{mn} and μ, ν:

$$\gamma_{mn} = \frac{e^{-\nu(\rho_{mn})d_o} - e^{-2\mu d_o}}{1 - e^{-2\mu d_o}}, \quad m, n = 1, \ldots, N. \tag{40}$$

We define $\mathbf{\Gamma}$ as the $N \times N$ matrix with elements γ_{mn}. The second moment extinction coefficient $\nu(\rho_{mn})$ is a monotonically increasing function, with $\nu(0) = 0$ and $\nu(\infty) = 2\mu$, so $\gamma_{mn} \in [0, 1]$.

Combining (31) and (32) into vectors, and using (36) yields

$$\widetilde{\mathbf{z}}(t) = \sqrt{S}\, e^{j\theta}\, e^{-\mu d_o}\, \mathbf{a} \; + \; e^{j\theta}\, \mathbf{a}\, \widetilde{\mathbf{v}}(t) \; + \; \widetilde{\mathbf{w}}(t), \tag{41}$$

where θ is defined in (21) and $\mathbf{a}$ is the array steering vector in (20). We define the matrix $\mathbf{B}$ with elements

$$B_{mn} = \exp\left[-\nu(\rho_{mn})d_o\right], \tag{42}$$

and then we can extend the second-order moments in (22)-(25) to the case with scattering as

$$E\{\widetilde{\mathbf{z}}(t)\} = e^{-\mu d_o}\, \sqrt{S}\, e^{j\theta}\, \mathbf{a} \stackrel{\triangle}{=} \mathbf{m}_{\tilde{\mathbf{z}}} \tag{43}$$

$$\mathbf{R}_{\tilde{\mathbf{z}}}(\xi) = e^{-2\mu d_o}\, S\, \mathbf{a}\mathbf{a}^\dagger \; + \; S\left[\mathbf{B} \circ \left(\mathbf{a}\mathbf{a}^\dagger\right) - e^{-2\mu d_o}\, \mathbf{a}\mathbf{a}^\dagger\right] \frac{r_{\tilde{v}}(\xi)}{S\left(1 - e^{-2\mu d_o}\right)} \; + \; r_{\tilde{w}}(\xi)\, \mathbf{I} \tag{44}$$

$$\begin{aligned}\mathbf{G}_{\tilde{\mathbf{z}}}(f) = {} & e^{-2\mu d_o}\, S\, \mathbf{a}\mathbf{a}^\dagger\, \delta(f) \\ & + \; S\left[\mathbf{B} \circ \left(\mathbf{a}\mathbf{a}^\dagger\right) - e^{-2\mu d_o}\, \mathbf{a}\mathbf{a}^\dagger\right] \frac{G_{\tilde{v}}(f)}{S\left(1 - e^{-2\mu d_o}\right)} \; + \; G_{\tilde{w}}(f)\, \mathbf{I}\end{aligned} \tag{45}$$

$$E\{\widetilde{\mathbf{z}}(t)\widetilde{\mathbf{z}}(t)^\dagger\} = \mathbf{R}_{\tilde{\mathbf{z}}}(0) = S\, \mathbf{B} \circ \left(\mathbf{a}\mathbf{a}^\dagger\right) \; + \; \sigma_{\tilde{w}}^2\, \mathbf{I} \stackrel{\triangle}{=} \mathbf{C}_{\tilde{\mathbf{z}}} \; + \; \mathbf{m}_{\tilde{\mathbf{z}}}\, \mathbf{m}_{\tilde{\mathbf{z}}}^\dagger, \tag{46}$$

where $\circ$ denotes element-wise product between matrices. The normalizing quantity $S\left(1 - e^{-2\mu d_o}\right)$ that divides the autocorrelation $r_{\tilde{v}}(\xi)$ and the PSD $G_{\tilde{v}}(f)$ in (44) and (45) is equal to $r_{\tilde{v}}(0) = \int G_{\tilde{v}}(f)\, df$. Therefore the maximum of the normalized autocorrelation is 1, and the area under the normalized PSD is 1. The complex envelope samples $\widetilde{\mathbf{z}}(t)$ have the complex normal distribution $\mathrm{CN}\left(\mathbf{m}_{\tilde{\mathbf{z}}}, \mathbf{C}_{\tilde{\mathbf{z}}}\right)$, which is defined in (30). The mean vector and covariance matrix are given in (43) and (46), but we repeat them below for comparison with (29),

$$\mathbf{m}_{\tilde{\mathbf{z}}} = e^{-\mu d_o}\, \sqrt{S}\, e^{j\theta}\, \mathbf{a} \qquad \text{(with scattering)} \tag{47}$$

$$\mathbf{C}_{\tilde{\mathbf{z}}} = S\left[\mathbf{B} \circ \left(\mathbf{a}\mathbf{a}^\dagger\right) - e^{-2\mu d_o}\, \mathbf{a}\mathbf{a}^\dagger\right] \; + \; \sigma_{\tilde{w}}^2\, \mathbf{I} \qquad \text{(with scattering).} \tag{48}$$

Note that the scattering is negligible if $d_o \ll 1/(2\mu)$, in which case $e^{-2\mu d_o} \approx 1$ and $\Omega \approx 0$. Then most of the signal energy is in the mean, with $\mathbf{B} \approx \mathbf{1}\mathbf{1}^T$ and $\gamma_{mn} \approx 1$ in (40), since $\nu(\rho_{mn}) < 2\mu$. For larger values of the source range d_o, more of the signal energy is scattered, and $\mathbf{B}$ may deviate from $\mathbf{1}\mathbf{1}^T$ (and $\gamma_{mn} < 1$ for $m \neq n$) due to coherence losses between the sensors. At full saturation ($\Omega = 1$), $\mathbf{B} = \mathbf{\Gamma}$.

The scattering model in (41) may be formulated as multiplicative noise on the steering vector,

$$\widetilde{\mathbf{z}}(t) = \sqrt{S}\, e^{j\theta}\, \mathbf{a} \circ \left[e^{-\mu d_o}\, \mathbf{1} \; + \; \frac{\widetilde{\mathbf{v}}(t)}{\sqrt{S}} \right] \; + \; \widetilde{\mathbf{w}}(t) \; \stackrel{\triangle}{=} \; \sqrt{S}\, e^{j\theta}\, (\mathbf{a} \circ \widetilde{\mathbf{u}}(t)) \; + \; \widetilde{\mathbf{w}}(t). \tag{49}$$

The multiplicative noise process, $\widetilde{\mathbf{u}}(t)$, is complex normal with $\mathbf{m}_{\widetilde{\mathbf{u}}} = E\{\widetilde{\mathbf{u}}(t)\} = e^{-\mu d_o}\, \mathbf{1}$ and $E\{\widetilde{\mathbf{u}}(t)\, \widetilde{\mathbf{u}}(t)^\dagger\} = \mathbf{B}$, so the covariance matrix is $\mathbf{C}_{\widetilde{\mathbf{u}}} = \mathbf{B} - e^{-2\mu d_o}\, \mathbf{1}\mathbf{1}^T = \Omega \mathbf{\Gamma}$, where $\mathbf{\Gamma}$ has elements γ_{mn} in (40). The mean vector and covariance matrix in (47) and (48) may be represented as $\mathbf{m}_{\widetilde{\mathbf{z}}} = \sqrt{S}\, e^{j\theta}\, (\mathbf{a} \circ \mathbf{m}_{\widetilde{\mathbf{u}}})$ and $\mathbf{C}_{\widetilde{\mathbf{z}}} = S\, \left[\left(\mathbf{a}\mathbf{a}^\dagger \right) \circ \mathbf{C}_{\widetilde{\mathbf{u}}} \right] \, + \, \sigma_{\widetilde{w}}^2\, \mathbf{I}$.

2.4 Model for extinction coefficients

During the past several decades, considerable effort has been devoted to the modeling of wave propagation through random media. Theoretical models have been developed for the extinction coefficients of the first and second moments, μ and $\nu(\rho)$, along nearly line-of-sight paths. For general background, we refer the reader to [5, 27, 30, 10]. Here we consider some specific results relevant to turbulence effects on aeroacoustic arrays.

The extent that scattering affects array performance depends on many factors, including the wavelength of the sound, the propagation distance from the source to the sensor array, the spacing between the sensors, the strength of the turbulence (as characterized by the variance of the temperature and wind-velocity fluctuations), and the size range of the turbulent eddies. Turbulence in the near-ground atmosphere spans a vast range of spatial scales, from millimeters to hundreds of meters. If the sensor spacing ρ is small compared to the size ℓ of the smallest eddies (a case highly relevant to optics but not low-frequency acoustics), $\nu(\rho)$ is proportional to $k^2\rho^2$, where $k = \omega/c_0$ is the wavenumber of the sound and c_0 the ambient sound speed [27]. In this situation, the loss in coherence between sensors results entirely from turbulence-induced variability in the AOA. Of greater practical importance in acoustics are situations where $\rho \gg \ell$. The spacing ρ may be smaller or larger than $\mathcal{L}$, the size of the largest eddies.

When $\rho \gg \ell$ and $\rho \ll \mathcal{L}$, the sensor spacing resides in the *inertial subrange* of the turbulence [5]. Because the strength of turbulence increases with the size of the eddies, this case has qualitative similarities to $\rho \ll \ell$. The wavefronts impinging on the array have a roughly constant AOA over the aperture and the apparent bearing of the source varies randomly about the actual bearing. Increasing the separation between sensors can dramatically decrease the coherence. In contrast, when $\rho \gg \mathcal{L}$ is large, the wavefront distortions induced by the turbulence produce nearly uncorrelated signal variations at the sensors. In this case, further increasing separation does not affect coherence: it is "saturated" at a value determined by the strength of the turbulence, and therefore has an effect similar to additive, uncorrelated noise. These two extreme cases are illustrated in Fig. 3. The resulting behavior of $\nu(\rho)$ and B_{mn} (Eq. 42) are shown in Fig. 4.

The general results for the extinction coefficients of a spherically propagating wave, derived with the parabolic (narrow-angle) and Markov approximations, and assuming $\rho \gg \ell$, are [Ref. [10], Eqs. (7.60) and (7.71); Ref. [30], Eq. 20-28]:

$$\mu = \frac{\pi^2 k^2}{2} \int_0^\infty dK_\perp K_\perp \Phi_{\text{eff}}(K_\parallel = 0, K_\perp) = k^2 \sigma_{\text{eff}}^2 \mathcal{L}_{\text{eff}}/4, \tag{50}$$

$$\nu(\rho) = \pi^2 k^2 \int_0^1 dt \int_0^\infty dK_\perp K_\perp \left[1 - J_0(K_\perp \rho t)\right] \Phi_{\text{eff}}(K_\parallel = 0, K_\perp), \tag{51}$$

in which J_0 is the zeroth-order Bessel function of the first kind and $\mathbf{K} = \mathbf{K}_\parallel + \mathbf{K}_\perp$ is the turbulence wavenumber vector decomposed into components parallel and perpendicular to the propagation path. The quantities $\Phi_{\text{eff}}(\mathbf{K})$, σ_{eff}, and $\mathcal{L}_{\text{eff}}$ are the effective turbulence spectrum, effective variance, and effective integral length scale. (The integral length scale is a quantitative measure of the size of the largest eddies.) The spectrum is defined as

$$\Phi_{\text{eff}}(\mathbf{K}) = \frac{\Phi_T(\mathbf{K})}{T_0^2} + \frac{4\Phi_\upsilon(\mathbf{K})}{c_0^2}, \tag{52}$$

where T_0 is the ambient temperature, and the subscripts T and υ indicate the temperature and wind-velocity fields, respectively. The definition of the effective variance is the same, except with σ^2 replacing $\Phi(\mathbf{K})$. The effective integral length scale is defined as

$$\mathcal{L}_{\text{eff}} = \frac{1}{\sigma_{\text{eff}}} \left(\mathcal{L}_T \frac{\sigma_T^2}{T_0^2} + \mathcal{L}_\upsilon \frac{4\sigma_\upsilon^2}{c_0^2} \right). \tag{53}$$

For the case $\rho/\mathcal{L}_{\text{eff}} \gg 1$, the contribution from the term in (51) involving the Bessel function is small and one has $\nu(\rho) \to 2\mu$, as anticipated from the discussion after (40). When $\rho/\mathcal{L}_{\text{eff}} \ll 1$, the inertial-subrange properties of the turbulence come into play and one finds [Ref. [10], Eq. (7.87)]

$$\nu(\rho) = 0.137 \left(\frac{C_T^2}{T_0^2} + \frac{22}{3} \frac{C_\upsilon^2}{c_0^2} \right) k^2 \rho^{5/3}, \tag{54}$$

where C_T^2 and C_υ^2 are the *structure-function parameters* for the temperature and wind fields, respectively. The structure-function parameters represent the strength of the turbulence in the inertial subrange.

Note that the extinction coefficients for both moments depend quadratically on the frequency of the tone, regardless of the separation between the sensors. The quantities μ, C_T^2, C_υ^2, and $\mathcal{L}_{\text{eff}}$ each depend strongly on atmospheric conditions. Table 1 provides estimated values for typical atmospheric conditions based on the turbulence models in [24, 11]. These calculations were performed for a propagation path height of 2 m.

It is evident from Table 1 that the entire range of saturation parameter values from $\Omega \approx 0$ to $\Omega \approx 1$ may be encountered in aeroacoustic applications, which typically have source ranges from meters to kilometers. Also, saturation occurs at distances several times closer to the source in sunny conditions than in cloudy ones. In a typical scenario in aeroacoustics involving a sensor standoff distance of several hundred meters, saturation will be small only for frequencies of about 100 Hz and lower. At frequencies above 200 Hz or so, the signal is generally saturated and random fluctuations dominate.

Based on the values for C_T^2 and C_v^2 in Table 1, coherence of signals is determined primarily by wind-velocity fluctuations (as opposed to temperature), except for mostly sunny, light wind conditions. It may at first seem a contradiction that the first-moment extinction coefficient μ is determined mainly by cloud cover (which affects solar heating of the ground), as opposed to the wind speed. Indeed, the source distance d_0 at which a given value of Ω is obtain is several times longer in cloudy conditions than in sunny ones. This can be understood from the fact that cloud cover damps strong thermal plumes (such as those used by hang gliders and seagulls to stay aloft), which are responsible for wind-velocity fluctuations that strongly affect acoustic signals.

Interestingly, the effective integral length scale for the sound field usually takes on a value intermediate between the microphone separations within small arrays (around 1 m) and the spacing between typical network nodes (which may be 100 m or more). As a result, high coherence can be expected within small arrays. However, coherence between nodes in a widely spaced network will be quite small, particularly at frequencies above 200 Hz or so.

Figure 5 illustrates the coherence of the scattered signals, γ_{mn} in (40), as a function of the sensor separation, ρ. The extinction coefficient in (54) is computed at frequency $f = 50$ Hz and source range $d_o = 1,500$ m, with mostly sunny, light wind conditions from Table 1, so $\Omega = 0.95$. Note the coherence is nearly perfect for sensor separations $\rho < 1$ m, then the coherence declines steeply for larger separations.

2.5 Multiple frequencies and sources

The model in (49) is for a single source that emits a single frequency, $\omega = 2\pi f_o$ rad/s. The complex envelope processing in (2) and Figure 2 is a function of the source frequency. We can extend the model in (49) to the case of K sources that emit tones at L frequencies $\omega_1, \ldots, \omega_L$, as follows:

$$\widetilde{\mathbf{z}}(iT_s;\omega_l) = \sum_{k=1}^{K} \sqrt{S_k(\omega_l)}\, e^{j\theta_{k,l}}\ \left(\mathbf{a}_k(\omega_l) \circ \widetilde{\mathbf{u}}_k(iT_s;\omega_l)\right) \ + \ \widetilde{\mathbf{w}}(iT_s;\omega_l), \qquad \begin{array}{c} i = 1,\ldots,T \\ l = 1,\ldots,L \end{array} \tag{55}$$

$$= \left([\mathbf{a}_1(\omega_l) \ldots \mathbf{a}_K(\omega_l)] \circ [\widetilde{\mathbf{u}}_1(iT_s;\omega_l) \ldots \widetilde{\mathbf{u}}_K(iT_s;\omega_l)]\right) \begin{bmatrix} \sqrt{S_1(\omega_l)}\, e^{j\theta_{1,l}} \\ \vdots \\ \sqrt{S_K(\omega_l)}\, e^{j\theta_{K,l}} \end{bmatrix} \ + \ \widetilde{\mathbf{w}}(iT_s;\omega_l)$$

$$\stackrel{\triangle}{=} \left(\mathbf{A}(\omega_l) \circ \widetilde{\mathbf{U}}(iT_s;\omega_l)\right) \widetilde{\mathbf{p}}(\omega_l) \ + \ \widetilde{\mathbf{w}}(iT_s;\omega_l). \tag{56}$$

In (55), $S_k(\omega_l)$ is the average power of source k at frequency ω_l, $\mathbf{a}_k(\omega_l)$ is the steering vector for source k at frequency ω_l as in (20), $\widetilde{\mathbf{u}}_k(iT_s;\omega_l)$ is the scattering of source k at frequency ω_l at time sample i, and T is the number of time samples. In (56), the steering vector matrices $\mathbf{A}(\omega_l)$, the scattering matrices $\widetilde{\mathbf{U}}(iT_s;\omega_l)$, and the source amplitude vectors $\widetilde{\mathbf{p}}(\omega_l)$ for $l = 1,\ldots,L$ and $i = 1,\ldots,T$, are defined by the context. If the sample spacing T_s is chosen appropriately, then the samples at a given frequency ω_l are independent in time. We will also model the scattered signals at different frequencies as independent. Cross-frequency coherence has been previously studied theoretically and experimentally, with [8, 31] presenting experimental studies in the atmosphere. However, models for cross-frequency coherence in the atmosphere are at a very preliminary stage. It may be possible to revise the assumption of independent scattering at different frequencies as better models become available.

The covariance matrix at frequency ω_l is, by extending the discussion following (49),

$$\mathbf{C}_{\widetilde{\mathbf{z}}}(\omega_l) = \sum_{k=1}^{K} S_k(\omega_l)\, \Omega_k(\omega_l)\ \left[\mathbf{\Gamma}_k(\omega_l) \circ \left(\mathbf{a}_k(\omega_l)\mathbf{a}_k(\omega_l)^\dagger\right)\right] \ + \ \sigma_{\widetilde{w}}(\omega_l)^2\, \mathbf{I}, \tag{57}$$

where the scattered signals from different sources are assumed to be independent. If we assume full saturation ($\Omega_k(\omega_l) = 1$) and negligible coherence loss across the array aperture ($\mathbf{\Gamma}_k(\omega_l) = \mathbf{1}\mathbf{1}^T$), then the sensor signals in (55) have zero mean, and the covariance matrix in (57) reduces to the familiar correlation matrix of the form

$$\mathbf{R}_{\widetilde{\mathbf{z}}}(0;\omega_l) = E\left\{\widetilde{\mathbf{z}}(iT_s;\omega_l)\, \widetilde{\mathbf{z}}(iT_s;\omega_l)^\dagger\right\}$$

$$= \mathbf{A}(\omega_l)\, \mathbf{S}(\omega_l)\, \mathbf{A}(\omega_l)^\dagger \ + \ \sigma_{\widetilde{w}}(\omega_l)^2\, \mathbf{I} \qquad (\Omega_k(\omega_l) = 1 \text{ and no coherence loss}), \tag{58}$$

where $\mathbf{S}(\omega_l)$ is a diagonal matrix with $S_1(\omega_l), \ldots, S_K(\omega_l)$ along the diagonal.[1]

---

[1] For the fully saturated case with no coherence loss, we can relax the assumption that the scattered signals from different sources are independent by replacing the diagonal matrix $\mathbf{S}(\omega_l)$ in (58) with a positive semidefinite matrix with (m,n) element $\sqrt{S_m(\omega_l)S_n(\omega_l)} \cdot E\{\widetilde{u}_m(iT_s;\omega_l)\widetilde{u}_n(iT_s;\omega_l)^*\}$, where $\widetilde{u}_m(iT_s;\omega_l)$ is the scattered signal for source m.

3 Signal Processing

In this section, we discuss signal processing methods for aeroacoustic sensor networks. The signal processing takes into account the source and propagation models presented in the previous section, as well as minimization of the communication bandwidth between sensor nodes connected by a wireless link. We begin with angle of arrival (AOA) estimation using a single sensor array in Section 3.1. Then we discuss source localization with multiple sensor arrays in Section 3.2, and we briefly describe implications for tracking, detection, and classification algorithms in Sections 3.3 and 3.4.

3.1 Angle of arrival estimation

We discuss narrowband AOA estimation with scattering in Section 3.1.1, and then we discuss wideband AOA estimation without scattering in Section 3.1.2.

3.1.1 Narrowband AOA estimation with scattering

In this section, we review some performance analyses and algorithms that have been investigated for narrowband AOA estimation with scattering. Most of the methods are based on scattering models that are similar to the single-source model in Section 2.3 or the multiple-source model in Section 2.5 at a single frequency. Many of the references cited below are formulated for radio frequency (RF) channels, so the equivalent channel effect is caused by multipath propagation and Doppler. The models for the RF case are similar to those presented in Section 2.

Wilson [21] analyzed the Cramér-Rao bound (CRB) on AOA estimation for a single source using several models for atmospheric turbulence. Rayleigh signal fading was assumed. Collier and Wilson extended the work [22, 23] to include unknown turbulence parameters in the CRB, along with the source AOA. Their CRB analysis provides insight into the combinations of atmospheric conditions, array geometry, and source location that are favorable for accurate AOA estimation. They note that refraction effects make it difficult to accurately estimate the elevation angle when the source and sensors are near the ground, so aeroacoustic sensor arrays are most effective for azimuth estimation.

Other researchers that have investigated the problem of imperfect spatial coherence in the context of narrowband AOA estimation include [32]–[40]. Paulraj and Kailath [32] presented a MUSIC algorithm that incorporates nonideal spatial coherence, assuming that the coherence losses are known. Song and Ritcey [33] provided maximum-likelihood (ML) methods for estimating the angles of arrival and the parameters in a coherence model. Gershman et al. [34] provided a procedure to jointly estimate the spatial coherence loss and the angles of arrival. In the series of papers [35]–[38], stochastic and deterministic models were studied for imperfect spatial coherence, and the performance of various AOA estimators was analyzed. Ghogho and Swami [39] presented an algorithm for AOA estimation with multiple sources in the fully-saturated case. Their algorithm exploits the Toeplitz structure of the $\mathbf{B}$ matrix in (42) for a uniform linear array (ULA).

None of the references [32]–[39] handle range of scattering scenarios from weak ($\Omega = 0$) to strong ($\Omega = 1$). Fuks, Goldberg, and Messer [40] treat the case of Rician scattering on RF channels, so this approach does include the entire range from weak to strong scattering. Indeed, the "Rice factor" in the Rician fading model is related to the saturation parameter through $(1 - \Omega)/\Omega$. The main focus in [40] is on CRBs for AOA estimation.

3.1.2 Wideband AOA estimation without scattering

Narrow band processing in the aeroacoustic context will limit the bandwidth to perhaps a few Hz, and the large fractional bandwidth encountered in aeroacoustics significantly complicates the array signal processing. A variety of methods are available for wideband AOA estimation, with varying complexity and applicability. Application of these to specific practical problems leads to a complicated task of appropriate procedure choice. We outline some of these methods and various tradeoffs, and describe some experimental results. Basic approaches include: classical delay-and-sum beamformer, incoherent averaging over narrow band spatial spectra, maximum likelihood, coherent signal subspace methods, steered matrix techniques, spatial resampling (array interpolation), and frequency-invariant beamforming. Useful overviews include Boehme [41], and Van Trees [42]. Significant progress in this area has occurred in the previous 15 years or so; major earlier efforts include the underwater acoustics area, e.g., see Owsley [43].

Using frequency decomposition at each sensor, we obtained the array data model in (55). For our discussion of wideband AOA methods, we will ignore the scattering, and so assume the spatial covariance can be written as in (58). Equation (58) may be interpreted as the covariance matrix of the Fourier-transformed (narrowband) observations (55). The noise is typically assumed to be Gaussian and spatially white, although generalizations to spatially correlated noise are also possible, which can be useful for modeling unknown spatial interference.

Working with an estimate $\hat{\mathbf{R}}_{\tilde{\mathbf{z}}}(0; \omega_l)$, we may apply covariance-based high resolution AOA estimators (MUSIC, MLE, etc.), although this results in many frequency-dependent angle estimates that must be associated in some way for each source. A simple approach is to sum the resulting narrowband spatial spectra, e.g., see [44]; this is referred to as *noncoherent averaging.* This approach has the advantages of straightforward extension of narrowband methods and relatively low complexity, but can produce artifacts. And, noncoherent averaging requires that the SNRs after channelization be adequate to support the chosen narrow band AOA estimator; in effect the method does not take strong advantage of the wideband nature of the signal. However, loud harmonic sources can be processed in this manner with success.

A more general approach was first developed by Wang and Kaveh [45], based on the following additive composition of transformed narrowband covariance matrices,

$$\mathbf{R}_{scm}(\phi_i) = \sum_l \mathbf{T}(\phi_i, \omega_l)\, \mathbf{R}_{\tilde{\mathbf{z}}}(0; \omega_l)\, \mathbf{T}(\phi_i, \omega_l)^\dagger, \tag{59}$$

where ϕ_i is the ith AOA. $\mathbf{R}_{scm}(\phi_i)$ is referred to as the *steered covariance matrix* or the *focused wideband covariance matrix.* The transformation matrix $\mathbf{T}(\phi_i, \omega_l)$, sometimes called the *focusing matrix*, can be viewed as selecting delays to coincide with delay-sum beamforming, so that the transformation depends on both AOA and frequency. Viewed in another way, the transformation matrix acts to align the signal subspaces, so that the resulting matrix $\mathbf{R}_{scm}(\phi_i)$ has a rank one contribution from a wideband source at angle ϕ_i. Now, narrowband covariance-based AOA estimation methods may be applied to the matrix $\mathbf{R}_{scm}(\phi_i)$. This approach is generally referred to as the *coherent subspace method* (CSM). CSM has significant advantages: it can handle correlated sources (due to the averaging over frequencies), it averages over the entire source bandwidth, and has good statistical stability. On the other hand, it requires significant complexity, and as originally proposed requires pre-estimation of the AOAs which can lead to biased estimates [46]. (Valaee and Kabal [47] present an alternative formulation of focusing matrices for CSM using a two-sided transformation, attempting to reduce the bias associated with CSM.)

A major drawback to CSM is the dependence of $\mathbf{T}$ on the the AOA. The most general form requires generation and eigendecomposition of $\mathbf{R}_{scm}(\phi_i)$ for each look angle; this is clearly undesirable from a computational standpoint.[2] The dependence of $\mathbf{T}$ on ϕ_i can be removed in some cases by incorporating spatial interpolation, thereby greatly reducing the complexity. The basic ideas are established by Krolik and Swingler in [48]; for an overview (including CSM methods) see Krolik [49].

As an example, consider a uniform linear array (ULA) [48, 49], with $d = \lambda_i/2$ spacing. In order to process over another wavelength choice λ_j ($\lambda_j > \lambda_i$), we could spatially interpolate the

---

[2] In their original work, Wang and Kaveh relied on pre-estimates of the AOAs to lower the computational burden [45].

physical array to a virtual array with the desired spacing ($d_j = \lambda_j/2$). The spatial resampling approach adjusts the spatial sampling interval d as a function of source wavelength λ_j. The result is a simplification of (59) to

$$\mathbf{R}_{sr} = \sum_{l} \mathbf{T}(\omega_l)\,\mathbf{R}_{\tilde{\mathbf{z}}}(0;\omega_l)\,\mathbf{T}(\omega_l)^{\dagger}, \tag{60}$$

where the angular dependence is now removed. The resampling acts to align the signal subspace contributions over frequency, so that a single wideband source results in a rank one contribution to $\mathbf{R}_{sr}$. Note that the spatial resampling is implicit in (60) via the matrices $\mathbf{T}(\omega_l)$. Conventional narrow band AOA estimation methods may now be applied to $\mathbf{R}_{sr}$ and, in contrast to CSM, this operation is conducted once for all angles.

Extensions of [48] from ULAs to arbitrary array geometries can be undertaken, but the dependence on look angle returns, and the resulting complexity is then similar to the CSM approaches. To avoid this, Friedlander and Weiss considered spatial interpolation of an arbitrary physical array to virtual arrays that are uniform and linear [50], thereby returning to a formulation like (60). Doron et al. [51] developed a spatial interpolation method for forming a focused covariance matrix with arbitrary arrays. The formulation relies on a truncated series expansion of plane waves in polar coordinates. The array manifold vector is now separable, allowing focusing matrices that are not a function of angle. The specific case of a *circular* array leads to an FFT-based implementation that is appealing due to its relatively low complexity.

While the spatial resampling methods are clearly desirable from a complexity standpoint, experiments indicate that they break down as the fractional bandwidth grows (see the examples that follow). This depends on the particular method, and the original array geometry. This may be due to accumulated interpolation error, undersampling, and calibration error. As we have noted, and show in our examples, fractional bandwidths of interest in aeroacoustics may easily exceed 100%. Thus, the spatial resampling methods should be applied with some caution in cases of large fractional bandwidth.

Alternatives to the CSM approach are also available. Many of these methods incorporate time domain processing, and so may avoid the frequency decomposition (DFT) associated with CSM. Buckley and Griffiths [52], and Agrawal and Prasad [53], have developed methods based on wideband correlation matrices. (The work of [53] generally relies on a white or near-white source spectrum assumption, and so might not be appropriate for harmonic sources.) Sivanand et al. [54, 55, 56] have shown that the CSM focusing can be achieved in the time domain, and treat the problem from a multichannel FIR filtering perspective. Another FIR based method employs frequency invariant beamforming, e.g., see Ward et al. [57] and references therein.

3.1.3 Performance analysis and wideband beamforming

Cramer-Rao bounds (CRBs) on wideband AOA estimation can be established using either a deterministic or random Gaussian source model, in additive Gaussian noise. The basic results were shown by Bangs [58]; see also Swingler [59]. The deterministic source case in (possibly colored) Gaussian noise is described in Kay [20]. Performance analysis of spatial resampling methods is considered by Friedlander and Weiss, who also provide CRBs, as well as a description of maximum-likehood wideband AOA estimation [50].

These CRBs typically require known source statistics, apply to unbiased estimates, and assume no scattering, whereas prior spectrum knowledge is usually not available, and the above wideband methods may result in biased estimates. Nevertheless, the CRB provides a valuable fundamental performance bound.

Basic extensions of narrow band beamforming methods are reviewed in Van Trees [42, chpt. 6], including delay-sum and wideband minimum variance distortionless response (MVDR) techniques. The CSM techniques also extend to wideband beamforming, e.g., see Yang and Kaveh [60].

3.1.4 AOA experiments

Next, we highlight some experimental examples and results, based on extensive aeroacoustic experiments carried out since the early 1990's [3, 61, 62, 63, 64, 65, 66]. These experiments were designed to test wideband superresolution AOA estimation algorithms based on array apertures of a few meters or less. The arrays were typically only approximately calibrated, roughly operating in $[50, 250]$ Hz, primarily circular in geometry, and planar (on the ground). Testing focused on military vehicles, and low flying rotary and fixed wing aircraft, and ground truth was typically obtained from GPS receivers on the sources.

Early results showed that superresolution AOA estimates could be achieved at ranges of one to two kilometers [61], depending on the various propagation conditions and source loudness, and that non-coherent summation of narrowband MUSIC spatial signatures significantly outperforms conventional wideband delay-sum beamforming [62]. When the sources had strong harmonic structure, it was a straightforward matter to select the spectral peaks for narrowband AOA estimation. These experiments also verified that a piece-wise stationary assumption was valid over intervals approximately below one second, that the observed spatial coherence was good over apertures of a few meters or less, and that only rough calibration was required with relatively inexpensive microphones. Outlier AOA estimates were also observed, even in apparently high SNR and good propagation conditions. In some cases outliers composed 10% of the AOA estimates, but these were infrequent enough that a robust tracking algorithm can reject them.

Tests of the CSM method (CSM-MUSIC) were conducted with diesel engine vehicles exhibiting strong harmonic signatures [63], as well as turbine engines exhibiting broad, relatively flat spectral signatures [64]. The CSM-MUSIC approach was contrasted with noncoherent MUSIC. In both cases the M largest spectral bins were selected adaptively for each data block. CSM-MUSIC was implemented with focusing matrix $\mathbf{T}$ diagonal. For harmonic source signatures, the noncoherent MUSIC method was shown to outperform CSM-MUSIC in many cases, generally depending on the observed narrowband SNRs [63]. On the other hand, the CSM-MUSIC method displays good statistical stability at a higher computational cost. And, inclusion of lower SNR frequency bins in noncoherent MUSIC can lead to artifacts in the resulting spatial spectrum.

For the broadband turbine source, the CSM-MUSIC approach generally performed better than noncoherent MUSIC, due to the ability of CSM to capture the broad spectral spread of the source energy [64]. Figure 6 depicts a typical experiment with a turbine vehicle, showing AOA estimates over a 250 second span, where the vehicle traverses approximately a ±1 kilometer path past the array. The largest $M = 20$ frequency bins were selected for each estimate. The AOA estimates (circles) are overlaid on GPS ground truth (solid line). The AOA estimators break down at the farthest ranges (the beginning and end of the data). Numerical comparison with the GPS-derived AOA's reveals the CSM-MUSIC to have slightly lower mean square error. While the three AOA estimators shown in Figure 6 for this single source case have roughly the same performance, we emphasize that examination of the beam patterns reveals that the CSM-MUSIC method exhibits the best statistical stability and lower sidelobe behavior over the entire data set [64]. In addition, the CSM-MUSIC approach exhibited better performance in multiple source testing.

Experiments with the spatial resampling approaches reveal that they require spatial oversampling to handle large fractional bandwidths [65, 66]. For example, the array manifold interpolation (AMI) method of Doron et al. [51] was tested experimentally and via simulation using a 12-element uniform circular array. While the CSM-MUSIC approach was asymptotically efficient in simulation, the AMI technique did not achieve the CRB. The AMI algorithm performance degraded as the fractional bandwidth was increased for a fixed spatial sampling rate. While the AMI approach is appealing from a complexity standpoint, effective application of AMI requires careful attention to the fractional bandwidth, maximum source frequency, array aperture, and degree of oversampling. Generally, the AMI approach required higher spatial sampling when compared to CSM type methods, and so AMI lost some of its potential complexity savings in both hardware and software.

3.2 Localization with distributed sensor arrays

The previous subsection was concerned with AOA estimation using a single sensor array. The (x, y) location of a source in the plane may be estimated efficiently using multiple sensor arrays that are distributed over a wide area. We consider source localization in this section using a network of sensors that are placed in an "array of arrays" configuration, as illustrated in Figure 7. Each array contains local processing capability and a wireless communication link with a fusion center. A standard approach for estimating the source locations involves AOA estimation at the individual arrays, communication of the bearings to the fusion center, and triangulation of the bearing estimates at the fusion center (e.g., see [67, 68, 69, 70, 71]). This approach is characterized by low communication bandwidth and low complexity, but the localization accuracy is generally inferior to the optimal solution in which the fusion center jointly processes all of the sensor data. The optimal solution requires high communication bandwidth and high processing complexity. The amount of improvement in localization accuracy that is enabled by greater communication bandwidth and processing complexity is dependent on the scenario, which we characterize in terms of the power spectra (and bandwidth) of the signals and noise at the sensors, the coherence between the source signals received at widely separated sensors, and the observation time (amount of data).

We have studied this scenario in [16], where a framework is presented to identify situations that have the potential for improved localization accuracy relative to the standard bearings-only triangulation method. We proposed an algorithm that is bandwidth-efficient and nearly optimal that uses beamforming at small-aperture sensor arrays and time-delay estimation (TDE) between widely-separated sensors. Accurate TD estimates using widely-separated sensors are utilized to achieve improved localization accuracy relative to bearings-only triangulation, and the scattering of acoustic signals by the atmosphere significantly impacts the accuracy of TDE. We provide a detailed study of TDE with scattered signals that are *partially* coherent at widely-spaced sensors in [16]. Our results quantify the scenarios in which TDE is feasible as a function of signal coherence, SNR per sensor, fractional bandwidth of the signal, and time-bandwidth product of the observed data. The basic result is that for a given SNR, fractional bandwidth, and time-bandwidth product, there exists a "threshold coherence" value that must be exceeded in order for TDE to achieve the CRB. The analysis is based on Ziv-Zakai bounds for TDE, expanding upon the results in [72, 73]. Time synchronization is required between the arrays for TDE.

Previous work on source localization with aeroacoustic arrays has focused on angle of arrival estimation with a *single* array, e.g., [61]-[66], [74, 75], as discussed in Section 3.1. The problem of imperfect spatial coherence in the context of narrowband angle-of-arrival estimation with a single array was studied in [21], [22, 23], [32]–[40], as discussed in Section 3.1.1. The problem of decentralized array processing was studied in [76]-[77]. Wax and Kailath [76] presented subspace algorithms for narrowband signals and distributed arrays, assuming perfect spatial coherence across each array but neglecting any spatial coherence that may exist between arrays. Stoica, Nehorai, and Soderstrom [77] considered maximum likelihood angle of arrival estimation with a large, perfectly coherent array that is partitioned into subarrays. Weinstein [78] presented performance analysis for pairwise processing of the wideband sensor signals from a single array, and he showed that pairwise processing is nearly optimal when the SNR is high. In [79], Moses et. al. studied autocalibration of sensor arrays, where for aeroacoustic arrays the loss of signal coherence at widely-separated sensors impacts the performance of autocalibration.

The results in [16] are distinguished from those cited in the previous paragraph in that the primary focus is a performance analysis that explicitly models partial spatial coherence in the signals at *different* sensor arrays in an array of arrays configuration, along with an analysis of decentralized processing schemes for this model. The previous works have considered wideband processing of aeroacoustic signals using a single array with perfect spatial coherence [61]-[66], [74, 75], imperfect spatial coherence across a single array aperture [21], [22, 23], [32]–[40], and decentralized processing with either zero coherence between distributed arrays [76] or full coherence between all sensors [77, 78]. We summarize the key results from [16] in Sections 3.2.1–3.2.3.

Source localization using the method of travel-time tomography is described in [80, 81]. In this type of tomography, TDEs are formed by cross correlating signals from widely spaced sensors. The TDEs are incorporated into a general inverse procedure that provides information on the atmospheric wind and temperature fields in addition to the source location. The tomography thereby adapts to time delay shifts that result from the intervening atmospheric structure.

Ferguson [82] describes localization of small-arms fire using the near-field wavefront curvature. The range and bearing of the source are estimated from two adjacent sensors. Ferguson's experimental results clearly illustrate random localization errors induced by atmospheric turbulence. In a separate article, Ferguson [83] discusses time-scale compression to compensate TDEs for differential Doppler resulting from fast-moving sources.

3.2.1 Model for array of arrays

Our model for the array of arrays scenario in Figure 7 is a wideband extension of the single-array, narrowband model in Section 2. Our array of arrays model includes two key assumptions.

1. The distance from the source to each array is sufficiently large so that the signals are fully saturated, i.e., $\Omega^{(h)}(\omega) \approx 1$ for $h = 1, \ldots, H$ and all ω. Therefore according to the model in Section 2.3, the sensor signals have zero mean.

2. Each array aperture is sufficiently small so that the coherence loss is negligible between sensor pairs in the array. For the example in Figure 5, this approximation is valid for array apertures less than 1 m.

It may be useful to relax these assumptions in order to consider the effects of nonzero mean signals and coherence losses across individual arrays. However, these assumptions allow us to focus on the impact of coherence losses in the signals at *different* arrays.

As in Section 2.1, we let (x_s, y_s) denote the coordinates of a single non-moving source, and we consider H arrays that are distributed in the same plane, as illustrated in Figure 7. Each array $h \in \{1, \ldots, H\}$ contains N_h sensors and has a reference sensor located at coordinates (x_h, y_h). The location of sensor $n \in \{1, \ldots, N_h\}$ is at $(x_h + \Delta x_{hn}, y_h + \Delta y_{hn})$, where $(\Delta x_{hn}, \Delta y_{hn})$ is the relative location with respect to the reference sensor. If c is the speed of propagation, then the propagation time from the source to the reference sensor on array h is

$$\tau_h = \frac{d_h}{c} = \frac{1}{c}\left[(x_s - x_h)^2 + (y_s - y_h)^2\right]^{1/2}, \tag{61}$$

where d_h is the distance from the source to array h, as in (5). We model the wavefronts over individual array apertures as perfectly coherent plane waves, so in the far-field approximation, the propagation time from the source to sensor n on array h is expressed by $\tau_h + \tau_{hn}$, where

$$\tau_{hn} \approx -\frac{1}{c}\left[\frac{x_s - x_h}{d_h}\Delta x_{hn} + \frac{y_s - y_h}{d_h}\Delta y_{hn}\right] = -\frac{1}{c}\left[(\cos\phi_h)\Delta x_{hn} + (\sin\phi_h)\Delta y_{hn}\right] \tag{62}$$

is the propagation time from the reference sensor on array h to sensor n on array h, and ϕ_h is the bearing of the source with respect to array h. Note that while the far-field approximation (62) is reasonable over individual array apertures, the wavefront curvature that is inherent in (61) must be retained in order to model wide separations between arrays.

The time signal received at sensor n on array h due to the source will be denoted as $s_h(t - \tau_h - \tau_{hn})$, where the vector $\mathbf{s}(t) = [s_1(t), \ldots, s_H(t)]^T$ contains the signals received at the reference sensors on the H arrays. The elements of $\mathbf{s}(t)$ are modeled as real-valued, continuous-time, zero-mean, jointly wide-sense stationary, Gaussian random processes with $-\infty < t < \infty$. These processes are fully specified by the $H \times H$ cross-correlation matrix

$$\mathbf{R}_s(\xi) = E\{\mathbf{s}(t+\xi)\,\mathbf{s}(t)^T\}. \tag{63}$$

The (g,h) element in (63) is the cross-correlation function

$$r_{s,gh}(\xi) = E\{s_g(t+\xi)\,s_h(t)\} \tag{64}$$

between the signals received at arrays g and h. The correlation functions (63) and (64) are equivalently characterized by their Fourier transforms, which are the cross-spectral density (CSD) functions in (65) and CSD matrix in (66),

$$\begin{aligned} G_{s,gh}(\omega) &= \mathcal{F}\{r_{s,gh}(\xi)\} = \int_{-\infty}^{\infty} r_{s,gh}(\xi)\exp(-j\omega\xi)\,d\xi && (65)\\ \mathbf{G}_s(\omega) &= \mathcal{F}\{\mathbf{R}_s(\xi)\}. && (66) \end{aligned}$$

The diagonal elements $G_{s,hh}(\omega)$ of (66) are the power spectral density (PSD) functions of the signals $s_h(t)$, and hence they describe the distribution of average signal power with frequency. The model allows the PSD to vary from one array to another to reflect differences in transmission loss and source aspect angle.

The off-diagonal elements of (66), $G_{s,gh}(\omega)$, are the CSD functions for the signals $s_g(t)$ and $s_h(t)$ received at distinct arrays $g \neq h$. In general, the CSD functions have the form

$$G_{s,gh}(\omega) = \gamma_{s,gh}(\omega)\ \left[G_{s,gg}(\omega)G_{s,hh}(\omega)\right]^{1/2}, \tag{67}$$

where $\gamma_{s,gh}(\omega)$ is the *spectral coherence function* for the signals, which has the property $0 \leq |\gamma_{s,gh}(\omega)| \leq 1$. Coherence magnitude $|\gamma_{s,gh}(\omega)| = 1$ corresponds to perfect correlation between the signals at arrays g and h, while the partially coherent case $|\gamma_{s,gh}(\omega)| < 1$ models random scattering in the propagation paths from the source to arrays g and h. Note that our assumption of perfect spatial coherence across individual arrays implies that the scattering has negligible impact on the intra-array delays τ_{hn} in (62) and the bearings $\phi_1, \ldots \phi_H$. The coherence $\gamma_{s,gh}(\omega)$ in (67) is an extension of the narrowband, short-baseline coherence γ_{mn} in (39). However, the relation to extinction coefficients in (40) is not necessarily valid for very large sensor separations.

The signal received at sensor n on array h is the delayed source signal plus noise,

$$z_{hn}(t) = s_h(t - \tau_h - \tau_{hn}) + w_{hn}(t), \tag{68}$$

where the noise signals $w_{hn}(t)$ are modeled as real-valued, continuous-time, zero-mean, jointly wide-sense stationary, Gaussian random processes that are mutually uncorrelated at distinct sensors, and are uncorrelated from the signals. That is, the noise correlation properties are

$$E\{w_{gm}(t+\xi)w_{hn}(t)\} \;=\; r_w(\xi)\,\delta_{gh}\delta_{mn} \quad \text{and} \quad E\{w_{gm}(t+\xi)s_h(t)\} = 0, \tag{69}$$

where $r_w(\xi)$ is the noise autocorrelation function, and the noise PSD is $G_w(\omega) = \mathcal{F}\{r_w(\xi)\}$. We then collect the observations at each array h into $N_h \times 1$ vectors $\mathbf{z}_h(t) = [z_{h1}(t), \ldots, z_{h,N_h}(t)]^T$ for $h = 1, \ldots, H$, and we further collect the observations from the H arrays into a vector

$$\mathbf{Z}(t) = \begin{bmatrix} \mathbf{z}_1(t)^T & \cdots & \mathbf{z}_H(t)^T \end{bmatrix}^T. \tag{70}$$

The elements of $\mathbf{Z}(t)$ in (70) are zero-mean, jointly wide-sense stationary, Gaussian random processes. We can express the CSD matrix of $\mathbf{Z}(t)$ in a convenient form with the following definitions. We denote the array steering vector for array h at frequency ω as

$$\mathbf{a}^{(h)}(\omega) = \begin{bmatrix} \exp(-j\omega\tau_{h1}) \\ \vdots \\ \exp(-j\omega\tau_{h,N_h}) \end{bmatrix} = \begin{bmatrix} \exp\left[j\frac{\omega}{c}\left((\cos\phi_h)\Delta x_{h1} + (\sin\phi_h)\Delta y_{h1}\right)\right] \\ \vdots \\ \exp\left[j\frac{\omega}{c}\left((\cos\phi_h)\Delta x_{h,N_h} + (\sin\phi_h)\Delta y_{h,N_h}\right)\right] \end{bmatrix}, \tag{71}$$

using τ_{hn} from (62) and assuming that the sensors have omnidirectional response. Let us define the relative time delay of the signal at arrays g and h as

$$D_{gh} = \tau_g - \tau_h, \tag{72}$$

where τ_h is defined in (61). Then the CSD matrix of $\mathbf{Z}(t)$ in (70) has the form

$$\mathbf{G}_{\mathbf{Z}}(\omega) = \tag{73}$$

$$\begin{bmatrix} \mathbf{a}^{(1)}(\omega)\mathbf{a}^{(1)}(\omega)^\dagger G_{s,11}(\omega) & \cdots & \mathbf{a}^{(1)}(\omega)\mathbf{a}^{(H)}(\omega)^\dagger \exp(-j\omega D_{1H})G_{s,1H}(\omega) \\ \vdots & \ddots & \vdots \\ \mathbf{a}^{(H)}(\omega)\mathbf{a}^{(1)}(\omega)^\dagger \exp(+j\omega D_{1H})G_{s,1H}(\omega)^* & \cdots & \mathbf{a}^{(H)}(\omega)\mathbf{a}^{(H)}(\omega)^\dagger G_{s,HH}(\omega) \end{bmatrix} + G_w(\omega)\mathbf{I}.$$

Recall that the source CSD functions $G_{s,gh}(\omega)$ in (73) depend on the signal PSDs and spectral coherence $\gamma_{s,gh}(\omega)$ according to (67). Note that (73) depends on the source location parameters (x_s, y_s) through the bearings ϕ_h in $\mathbf{a}^{(h)}(\omega)$ and the pairwise time-delay differences D_{gh}.

3.2.2 Cramér-Rao bounds (CRBs) and examples

The problem of interest is estimation of the source location parameter vector $\mathbf{\Theta} = [x_s, y_s]^T$ using T independent samples of the sensor signals $\mathbf{Z}(0), \mathbf{Z}(T_s), \ldots, \mathbf{Z}((T-1)\cdot T_s)$, where T_s is the sampling period. The total observation time is $\mathcal{T} = T \cdot T_s$, and the sampling rate is $f_s = 1/T_s$ and $\omega_s = 2\pi f_s$. We will assume that the continuous-time random processes $\mathbf{Z}(t)$ are band-limited, and that the sampling rate f_s is greater than twice the bandwidth of the processes. Then it has been shown [84, 85] that the Fisher information matrix (FIM) $\mathbf{J}$ for the parameters $\mathbf{\Theta}$ based on the samples $\mathbf{Z}(0), \mathbf{Z}(T_s), \ldots, \mathbf{Z}((T-1) \cdot T_s)$ has elements

$$J_{ij} = \frac{\mathcal{T}}{4\pi} \int_0^{\omega_s} \mathrm{tr} \left\{ \frac{\partial \, \mathbf{G}_{\mathbf{Z}}(\omega)}{\partial \, \theta_i} \, \mathbf{G}_{\mathbf{Z}}(\omega)^{-1} \frac{\partial \, \mathbf{G}_{\mathbf{Z}}(\omega)}{\partial \, \theta_j} \, \mathbf{G}_{\mathbf{Z}}(\omega)^{-1} \right\} \, d\omega, \qquad i, j = 1, 2, \tag{74}$$

where "tr" denotes the trace of the matrix. The CRB matrix $\mathbf{C} = \mathbf{J}^{-1}$ then has the property that the covariance matrix of any unbiased estimator $\hat{\mathbf{\Theta}}$ satisfies $\mathrm{Cov}(\hat{\mathbf{\Theta}}) - \mathbf{C} \geq \mathbf{0}$, where $\geq \mathbf{0}$ means that $\mathrm{Cov}(\hat{\mathbf{\Theta}}) - \mathbf{C}$ is positive semidefinite. Equation (74) provides a convenient way to compute the FIM for the array of arrays model as a function of the signal coherence between distributed arrays, the signal and noise bandwidth and power spectra, and the sensor placement geometry.

The CRB presented in (74) provides a performance bound on source location estimation methods that *jointly* process all the data from all the sensors. Such processing provides the best attainable results, but also requires significant communication bandwidth to transmit data from the individual arrays to the fusion center. Next we develop approximate performance bounds on schemes that perform bearing estimation at the individual arrays in order to reduce the required communication bandwidth to the fusion center. These CRBs facilitate a study of the tradeoff between source location accuracy and communication bandwidth between the arrays and the fusion center. The methods that we consider are summarized as follows.

1. Each array estimates the source bearing, transmits the bearing estimate to the fusion center, and the fusion processor triangulates the bearings to estimate the source location. This approach does not exploit wavefront coherence between the distributed arrays, but it greatly reduces the communication bandwidth to the fusion center.

2. The raw data from all sensors is jointly processed to estimate the source location. This is the optimum approach that fully utilizes the coherence between distributed arrays, but it requires large communication bandwidth.

3. Combination of methods 1 and 2, where each array estimates the source bearing and transmits the bearing estimate to the fusion center. In addition, the raw data from *one sensor* in each array is transmitted to the fusion center. The fusion center estimates the propagation time delay between pairs of distributed arrays, and processes these time delay estimates with the bearing estimates to localize the source.

Next we evaluate CRBs for the three schemes for a narrowband source and a wideband source. Consider $H = 3$ identical arrays, each of which contains $N_1 = \cdots = N_H = 7$ sensors. Each array is circular with 4-ft radius, and six sensors are equally spaced around the perimeter and one sensor is in the center. We first evaluate the CRB for a narrowband source with a 1 Hz bandwidth centered at 50 Hz and SNR = 10 dB at each sensor. That is, $G_{s,hh}(\omega)/G_w(\omega) = 10$ for $h = 1, \ldots, H$ and $2\pi(49.5) < \omega < 2\pi(50.5)$ rad/sec. The signal coherence $\gamma_{s,gh}(\omega) = \gamma_s(\omega)$ is varied between 0 and 1. We assume that $T = 4000$ time samples are obtained at each sensor with sampling rate $f_s = 2000$ samples/sec. The source localization performance is evaluated by computing the ellipse in (x, y) coordinates that satisfies the expression $\begin{bmatrix} x & y \end{bmatrix} \mathbf{J} \begin{bmatrix} x \\ y \end{bmatrix} = 1$, where $\mathbf{J}$ is the FIM in (74). If the errors in (x, y) localization are jointly Gaussian distributed, then the ellipse represents the contour at one standard deviation in root-mean-square (RMS) error. The error ellipse for any unbiased estimator of source location cannot be smaller than this ellipse derived from the FIM.

The $H = 3$ arrays are located at coordinates $(x_1, y_1) = (0, 0)$, $(x_2, y_2) = (400, 400)$, and $(x_3, y_3) = (100, 0)$, where the units are meters. One source is located at $(x_s, y_s) = (200, 300)$, as illustrated in Figure 8a. The RMS error ellipses for joint processing of all sensor data for coherence values $\gamma_s(\omega) = 0, 0.5$, and 1 are also shown in Figure 8a. The coherence between all pairs of arrays is assumed to be identical, i.e., $\gamma_{s,gh}(\omega) = \gamma_s(\omega)$ for $(g, h) = (1, 2), (1, 3), (2, 3)$. The largest ellipse in Figure 8a corresponds to incoherent signals, i.e., $\gamma_s(\omega) = 0$, and characterizes the performance of the simple method of triangulation using the bearing estimates from the three arrays. Figure 8b shows the ellipse radius $= \left[(\text{major axis})^2 + (\text{minor axis})^2\right]^{1/2}$ for various values of the signal coherence $\gamma_s(\omega)$. The ellipses for $\gamma_s(\omega) = 0.5$ and 1 are difficult to see in Figure 8a because they fall on the lines of the × that marks the source location, illustrating that signal coherence between the arrays significantly improves the CRB on source localization accuracy. Note also that for this scenario, the localization scheme based on bearing estimation with each array and time-delay estimation using one sensor from each array has the same CRB as the optimum, joint processing scheme. Figure 8c shows a closer view of the error ellipses for the scheme of bearing estimation plus time-delay estimation with one sensor from each array. The ellipses are identical to those in Figure 8a for joint processing.

Figures 8d– 8f present corresponding results for a wideband source with bandwidth 20 Hz centered at 50 Hz and SNR 16 dB. That is, $G_{s,hh}/G_w = 40$ for $2\pi(40) < \omega < 2\pi(60)$ rad/sec, $h = 1, \ldots, H$. $T = 2000$ time samples are obtained at each sensor with sampling rate $f_s = 2000$ samples/sec, so the observation time is 1 second. As in the narrowband case in Figures 8a– 8c, joint processing reduces the CRB compared with bearings-only triangulation, and bearing plus time-delay estimation is nearly optimum.

The CRB provides a lower bound on the variance of unbiased estimates, so an important question is whether an estimator can *achieve* the CRB. We show next in Section 3.2.3 that the coherent processing CRBs for the narrowband scenario illustrated in Figures 8a– 8c are achievable only when the the coherence is perfect, i.e. $\gamma_s = 1$. Therefore for that scenario, bearings-only triangulation is optimum in the presence of even small coherence losses. However, for the wideband scenario illustrated in Figures 8d– 8f, the coherent processing CRBs are achievable for coherence values $\gamma_s \overset{\sim}{>} 0.75$.

3.2.3 TDE and examples

The CRB results presented in Section 3.2.2 indicate that time delay estimation between widely-spaced sensors may be an effective way to improve the source localization accuracy with joint processing. Fundamental performance limits for passive time delay and Doppler estimation have been studied extensively for several decades, e.g., see the collection of papers in [86]. The fundamental limits are usually parameterized in terms of the signal-to-noise ratio (SNR) at each sensor, the spectral support of the signals (fractional bandwidth), and the time-bandwidth product of the observations. However, the effect of coherence loss on TDE accuracy has not been explicitly considered.

In this section, we quantify the effect of partial signal coherence on time delay estimation. We present Cramér-Rao and Ziv-Zakai bounds that are explicitly parameterized by the signal coherence, along with the traditional parameters of SNR, fractional bandwidth, and time-bandwidth product. This analysis of TDE is relevant to method 3 in Section 3.2.2. We focus on the case of $H = 2$ sensors here. The extension to $H > 2$ sensors is outlined in [16].

Let us specialize (68) to the case of two sensors, with $H = 2$ and $N_1 = N_2 = 1$, so

$$z_1(t) = s_1(t) + w_1(t) \ \text{ and } \ z_2(t) = s_2(t - D) + w_2(t), \tag{75}$$

where $D = D_{21}$ is the differential time delay. Following (73), the CSD matrix is

$$\text{CSD}\begin{bmatrix} z_1(t) \\ z_2(t) \end{bmatrix} = \mathbf{G_Z}(\omega) = \tag{76}$$

$$\begin{bmatrix} G_{s,11}(\omega) + G_w(\omega) & e^{+j\omega D}\gamma_{s,12}(\omega)\,[G_{s,11}(\omega)G_{s,22}(\omega)]^{1/2} \\ e^{-j\omega D}\gamma_{s,12}(\omega)^*\,[G_{s,11}(\omega)G_{s,22}(\omega)]^{1/2} & G_{s,22}(\omega) + G_w(\omega) \end{bmatrix}.$$

The signal coherence function $\gamma_{s,12}(\omega)$ describes the degree of correlation that remains in the signal emitted by the source at each frequency ω after propagating to sensors 1 and 2.

We consider the following simplified scenario. The signal and noise spectra are flat over a bandwidth of $\Delta\omega$ rad/sec centered at ω_0 rad/sec, the observation time is $\mathcal{T}$ sec, and the propagation is fully saturated, so the signal mean is zero. Further, the signal PSDs are identical at each sensor, and we define the following constants for notational simplicity:

$$G_{s,11}(\omega_0) = G_{s,22}(\omega_0) = G_s,\ G_w(\omega_0) = G_w,\ \text{and}\ \gamma_{s,12}(\omega_0) = \gamma_s. \tag{77}$$

Then we can use (76) in (74) to find the CRB for TDE with $H = 2$ sensors, yielding

$$\begin{aligned} \text{CRB}(D) &= \frac{1}{2\omega_0^2\left(\frac{\Delta\omega\mathcal{T}}{2\pi}\right)\left[1+\frac{1}{12}\left(\frac{\Delta\omega}{\omega_0}\right)^2\right]}\left[\frac{1}{|\gamma_s|^2}\left(1+\frac{1}{(G_s/G_w)}\right)^2 - 1\right] & (78)\\ &> \frac{1}{2\omega_0^2\left(\frac{\Delta\omega\mathcal{T}}{2\pi}\right)\left[1+\frac{1}{12}\left(\frac{\Delta\omega}{\omega_0}\right)^2\right]}\left[\frac{1}{|\gamma_s|^2} - 1\right]. & (79)\end{aligned}$$

The quantity $\left(\frac{\Delta\omega\cdot\mathcal{T}}{2\pi}\right)$ is the time-bandwidth product of the observations, $\left(\frac{\Delta\omega}{\omega_0}\right)$ is the fractional bandwidth of the signal, and G_s/G_w is the SNR at each sensor. Note from the high-SNR limit in (79) that when the signals are partially coherent, so that $|\gamma_s| < 1$, increased source power does not reduce the CRB. Improved TDE accuracy is obtained with partially coherent signals by increasing the observation time $\mathcal{T}$ or changing the spectral support of the signal, which is $[\omega_0 - \Delta\omega/2, \omega_0 + \Delta\omega/2]$. The spectral support of the signal is not controllable in passive TDE applications, so increased observation time is the only means for improving the TDE accuracy with partially coherent signals. Source motion becomes more important during long observation times, as we discuss in Section 3.3.

We have shown in [16] that the CRB on TDE is achievable only when the coherence, γ_s, exceeds a threshold. The analysis is based on Ziv-Zakai bounds as in [72, 73], and the result is that the coherence must satisfy the following inequality in order for the CRB on TDE in (78) to be achievable:

$$|\gamma_s|^2 \geq \frac{\left(1+\frac{1}{(G_s/G_w)}\right)^2}{1+\frac{1}{\text{SNR}_{\text{thresh}}}}, \quad \text{so} \quad |\gamma_s|^2 \geq \frac{1}{1+\frac{1}{\text{SNR}_{\text{thresh}}}} \quad \text{as} \quad \frac{G_s}{G_w} \to \infty. \tag{80}$$

The quantity $\text{SNR}_{\text{thresh}}$ is

$$\text{SNR}_{\text{thresh}} = \frac{6}{\pi^2\left(\frac{\Delta\omega\mathcal{T}}{2\pi}\right)}\left(\frac{\omega_0}{\Delta\omega}\right)^2\left[\varphi^{-1}\left(\frac{1}{24}\left(\frac{\Delta\omega}{\omega_0}\right)^2\right)\right]^2 \tag{81}$$

where $\varphi(y) = 1/\sqrt{2\pi}\int_y^\infty \exp(-t^2/2)\,dt$. Since $|\gamma_s|^2 \leq 1$, (80) is useful only if $G_s/G_w > \text{SNR}_{\text{thresh}}$. Note that the threshold coherence value in (80) is a function of the time-bandwidth product, $\left(\frac{\Delta\omega\cdot\mathcal{T}}{2\pi}\right)$, and the fractional bandwidth, $\left(\frac{\Delta\omega}{\omega_0}\right)$, through the formula for $\text{SNR}_{\text{thresh}}$ in (81).

Figure 9a contains a plot of (80) for a particular case in which the signals are in a band centered at $\omega_0 = 2\pi 50$ rad/sec and the time duration is $\mathcal{T} = 2$ seconds. Figure 9a shows the variation in threshold coherence as a function of signal bandwidth, $\Delta\omega$. Note that nearly perfect coherence is required when the signal bandwidth is less than 5 Hz (or 10% fractional bandwidth). The threshold coherence drops sharply for values of signal bandwidth greater than 10 Hz (20% fractional bandwidth). Thus for sufficiently wideband signals, e.g., $\Delta\omega \geq 2\pi 10$ rad/sec, a certain amount of coherence loss can be tolerated while still allowing unambiguous time delay estimation. Figure 9b shows corresponding results for a case with twice the center frequency and half the observation time. Figure 9c shows the threshold coherence as a function of the time-bandwidth product and the fractional bandwidth for large SNR, $\frac{G_s}{G_w} \to \infty$. Note that very large time-bandwidth product is required to overcome coherence loss when the fractional bandwidth is small. For example, if the fractional bandwidth is 0.1, then the time-bandwidth product must exceed 100 if the coherence is 0.9. For threshold coherence values in the range from about 0.1 to 0.9, each doubling of the fractional bandwidth reduces the required time-bandwidth product by a factor of 10.

Let us examine a scenario that is typical in aeroacoustics, with center frequency $f_o = \omega_o/(2\pi) =$ 50 Hz and bandwidth $\Delta f = \Delta\omega/(2\pi) = 5$ Hz, so the fractional bandwidth is $\Delta f / f_o = 0.1$. From Figure 9c, signal coherence $|\gamma_s| = 0.8$ requires time-bandwidth product $\Delta f \cdot \mathcal{T} > 200$, so the necessary time duration $\mathcal{T} = 40$ sec for TDE is impractical for moving sources.

Larger time-bandwidth products of the observed signals are required in order to make TDE feasible in environments with signal coherence loss. As discussed previously, only the observation time is controllable in passive applications, thus leading us to consider source motion models in Section 3.3 for use during long observation intervals.

We can evaluate the threshold coherence for the narrowband and wideband scenarios considered in Section 3.2.2 for the CRB examples in Figure 8. The results are as follows, using (80) and (81).

- Narrowband case: $G_s/G_w = 10$, $\omega_0 = 2\pi 50$ rad/sec, $\Delta\omega = 2\pi$ rad/sec, $\mathcal{T} = 2$ sec
  $\Longrightarrow$ Threshold coherence ≈ 1
- Wideband case: $G_s/G_w = 40$, $\omega_0 = 2\pi 50$ rad/sec, $\Delta\omega = 2\pi \cdot 20$ rad/sec, $\mathcal{T} = 1$ sec
  $\Longrightarrow$ Threshold coherence ≈ 0.75

Therefore for the narrowband case, joint processing of the data from different arrays will not achieve the CRBs in Figures 8a– 8c when there is any loss in signal coherence. For the wideband case, joint processing can achieve the CRBs in Figures 8d– 8f for coherence values ≥ 0.75.

We have presented simulation examples in [16] that confirm the accuracy of the CRB in (78) and threshold coherence in (80). In particular, the simulations show that TDE based on cross-correlation processing achieves the CRB only when the threshold coherence is exceeded.

We conclude this section with a TDE example based on data that was measured by BAE Systems using a synthetically-generated, non-moving, wideband acoustic source. The source bandwidth is approximately 50 Hz with center frequency 100 Hz, so the fractional bandwidth is 0.5. Four nodes are labeled and placed in the locations shown in Figure 9a. The nodes are arranged in a triangle, with nodes on opposite vertices separated by about 330 ft, and adjacent vertices separated by about 230 ft. The source is at node 0, and receiving sensors are located at nodes 1, 2, and 3.

The PSDs estimated at sensors 1 and 3 are shown in Figure 10b, and the estimated coherence magnitude between sensors 1 and 3 is shown in Figure 10c. The PSDs and coherence are estimated using data segments of duration 1 second. Note that the PSDs are not identical due to differences in the propagation paths. The coherence magnitude exceeds 0.8 over an appreciable band centered at 100 Hz. The threshold coherence value from (80) for the parameters in this experiment is 0.5, so the actual coherence of 0.8 exceeds the threshold. Thus accurate TDE should be feasible, and indeed, we found that generalized cross-correlation yielded accurated TDE estimates. Differential time delays were estimated using the signals measured at nodes 1, 2, and 3, and the TDEs were hyperbolically triangulated to estimate the location of the source (which is at node 0). Figure 10d shows the hyperbolas obtained from the three differential time delay estimates, and Figure 10e shows an expanded view near the intersection point. The triangulated location is within 1 foot of the true source location, which is at $(-3, 0)$ feet.

This example shows the feasibility of TDE with acoustic signals measured at widely-separated sensors, provided that the SNR, fractional bandwidth, time-bandwidth product, and coherence meet the required thresholds. If the signal properties do not satisfy the thresholds, then then accurate TDE is not feasible and triangulation of AOAs is optimum.

3.3 Tracking moving sources

In this section, we summarize past work and key issues for tracking moving sources. A widely-studied approach for estimating the locations of moving sources with an array of arrays involves bearing estimation at the individual arrays, communication of the bearings to the fusion center, and processing of the bearing estimates at the fusion center with a tracking algorithm (e.g., see [67, 68, 69, 70, 71]).

As discussed in Section 3.2, jointly processing data from widely-spaced sensors has the potential for improved source localization accuracy, compared with incoherent triangulation/tracking of bearing estimates. The potential for improved accuracy depends directly on TDE between the sensors, which is feasible only with an increased time-bandwidth product of the sensor signals. This leads to a constraint on the minimum observation time, $\mathcal{T}$, in passive applications where the signal bandwidth is fixed. If the source is moving, then approximating it as non-moving becomes poorer as $\mathcal{T}$ increases, so modeling the source motion becomes more important.

Approximate bounds are known [87, 88] that specify the maximum time interval over which moving sources are may be approximated as nonmoving for TDE. We have applied the bounds to a typical scenario in aeroacoustics [89]. Let us consider $H = 2$ sensors, and a vehicle moving at 15 m/sec (about 5% the speed of sound), with radial motion that is in opposite directions at the two sensors. If the highest frequency of interest is 100 Hz, then the time interval over which the source is well-approximated as nonmoving is $\mathcal{T} \ll 0.1$ sec. According to the TDE analysis in Section 3.2, this yields insufficient time-bandwidth product for partially coherent signals that are typically encountered. Thus motion modeling and Doppler estimation/compensation are critical, even for aeroacoustic sources that move more slowly than in this example.

We have extended the model for a nonmoving source presented in Section 3.2 to a moving source with a first-order motion model in [89]. We have also presented an algorithm for estimating the motion parameters for multiple moving sources in [89], and the algorithm is tested with measured aeroacoustic data. The algorithm is initialized using the local polynomial approximation (LPA) beamformer [90] at each array to estimate the bearings and bearing rates. If the signals have sufficient coherence and bandwidth at the arrays, then the differential TDEs and Doppler shifts may be estimated. The maximum likelihood solution involves wideband ambiguity function search over Doppler and TDE [87], but computationally simpler alternatives have been investigated [91]. If TDE is not feasible, then the source may be localized by triangulating bearing, bearing rate, and differential Doppler. Interestingly, differential Doppler provides sufficient information for source localization, even without TDE, as long as five or more sensors are available [92]. Thus the source motion may be exploited via Doppler estimation in scenarios where TDE is not feasible, such as narrowband or harmonic signals.

Recent work on tracking multiple sources with aeroacoustic sensors include the penalized maximum likelihood approach in [75], and the α-β/Kalman tracking algorithms in [94]. It may be feasible to use source aspect angle differences and Doppler estimation to help solve the data association problem in multiple target tracking based on data from multiple sensor arrays.

3.4 Detection and classification

It is necessary to detect the presence of a source before carrying out the localization processing discussed in Sections 3.1, 3.2, and 3.3. Detection is typically performed by comparing the energy at a sensor with a threshold. The acoustic propagation model presented in Section 2 implies that the energy fluctuates due to scattering, so the scattering has a significant impact on detection algorithms and their performance.

In addition to detecting a source and localizing its position, it is desirable to identify (or classify) the type of vehicle from its acoustic signature. The objective is to broadly classify into categories such as “ground, tracked,” “ground, wheeled,” “airborne, fixed wing,” “airborne, rotary wing,” and to further identify the particular vehicle type within these categories. Most classification algorithms that have been developed for this problem use the relative amplitudes of harmonic components in the acoustic signal as features to distinguish between vehicle types [95]–[102]. However, the harmonic amplitudes for a given source may vary significantly due to several factors. The scattering model presented in Section 2 implies that the energy in each harmonic will randomly fluctuate due to scattering, and the fluctuations will be stronger at higher frequencies. The harmonic amplitudes may also vary with engine speed and the orientation of the source with respect to the sensor (aspect angle).

In this section, we specialize the scattering model from Section 2 to describe the probability distribution for the energy at a single sensor for a source with a harmonic spectrum. We then discuss the implications for detection and classification performance. More detailed discussions may be found in [25] for detection and [93] for classification.

The source spectrum is assumed to be harmonic, with energy at frequencies $\omega_1, \ldots, \omega_L$. Following the notation in Section 2.5 and specializing to the case of one source and one sensor, $S(\omega_l), \Omega(\omega_l)$, and $\sigma_{\widetilde{w}}^2(\omega_l)$ represent the average source power, the saturation, and the average noise power at frequency ω_l, respectively. The complex envelope samples at each frequency ω_l are then modeled with the first element of the vector in (55) with $K = 1$ source, and they have a complex Gaussian distribution,

$$\widetilde{z}(iT_s;\omega_l) \ \sim\ \mathrm{CN}\left(\sqrt{[1-\Omega(\omega_l)]\,S(\omega_l)}\,e^{j\theta(i;\omega_l)},\ \ \Omega(\omega_l)S(\omega_l)+\sigma_{\widetilde{w}}^2(\omega_l)\right), \quad \begin{array}{c} i=1,\ldots,T \\ l=1,\ldots,L \end{array}. \qquad (82)$$

The number of samples is T, and the phase $\theta(i;\omega_l)$ is defined in (21) and depends on the source phase and distance. We allow $\theta(i;\omega_l)$ to vary with the time sample index, i, in case the source phase (χ) or the source distance (d_o) changes. As discussed in Section 2.5, we model the complex Gaussian random variables in (82) as independent.

As discussed in Sections 2.3 and 2.4, the saturation (Ω) is related to the extinction coefficient of the first moment (μ) according to $\Omega(\omega_l) = 1 - \exp(-2\,\mu(\omega_l)\,d_o)$, where d_o is the distance from the source to the sensor. The dependence of the saturation on frequency and weather conditions is modeled by the following approximate formula for μ,

$$\mu(\omega) \approx \begin{cases} 4.03 \times 10^{-7} \left(\frac{\omega}{2\pi}\right)^2, & \text{mostly sunny} \\ 1.42 \times 10^{-7} \left(\frac{\omega}{2\pi}\right)^2, & \text{mostly cloudy} \end{cases}, \quad \frac{\omega}{2\pi} \in [30, 200] \text{ Hz}, \tag{83}$$

which is obtained by fitting (50) to the values for μ^{-1} in Table 1. A contour plot of the saturation as a function of frequency and source range is shown in Figure 11a using (83) for mostly sunny conditions. Note that the saturation varies significantly with frequency for ranges > 100 m. Larger saturation values imply more scattering, so the energy in the higher harmonics will fluctuate more widely than the lower harmonics.

We will let $P(\omega_1), \ldots, P(\omega_L)$ denote the estimated energy at each frequency. The energy may be estimated from the complex envelope samples in (82) by coherent or incoherent combining,

$$P_C(\omega_l) = \left| \frac{1}{T} \sum_{i=1}^{T} \widetilde{z}(iT_s; \omega_l) e^{-j\theta(i;\omega_l)} \right|^2, \qquad l = 1, \ldots, L \tag{84}$$

$$P_I(\omega_l) = \frac{1}{T} \sum_{i=1}^{T} \left| \widetilde{z}(iT_s; \omega_l) \right|^2, \qquad l = 1, \ldots, L. \tag{85}$$

Coherent combining is feasible only if the phase shifts $\theta(i;\omega_l)$ are known or are constant with i. Our assumptions imply that the random variables in (84) are independent over l, as are the random variables in (85). The probability distribution functions (pdfs) for P_C and P_I are noncentral chi-squared distributions[3]. We let $\chi^2(D, \delta)$ denote the *standard* noncentral chi-squared distribution with D degrees of freedom and noncentrality parameter δ. Then the random variables in (84) and (85) may be scaled so that their pdfs are standard noncentral chi-squared distributions,

$$\frac{P_C(\omega_l)}{\left[\Omega(\omega_l) S(\omega_l) + \sigma_{\tilde{w}}^2(\omega_l)\right] / (2T)} \sim \chi^2\left(2,\, \delta(\omega_l)\right) \tag{86}$$

$$\frac{P_I(\omega_l)}{\left[\Omega(\omega_l) S(\omega_l) + \sigma_{\tilde{w}}^2(\omega_l)\right] / (2T)} \sim \chi^2\left(2T,\, \delta(\omega_l)\right), \tag{87}$$

where the noncentrality parameter is

$$\delta(\omega_l) = \frac{\left[1 - \Omega(\omega_l)\right] S(\omega_l)}{\left[\Omega(\omega_l) S(\omega_l) + \sigma_{\tilde{w}}^2(\omega_l)\right] / (2T)}. \tag{88}$$

---

[3] The random variable $\sqrt{P_C}$ in (84) has a Rician distribution, which is widely used to model fading RF communication channels.

The only difference in the pdfs for coherent and incoherent combining is the number of degrees of freedom in the noncentral chi-squared pdf: 2 degrees of freedom for coherent, and $2T$ degrees of freedom for incoherent.

The noncentral chi-squared pdf is readily available in analytical form and in statistical software packages, so the performance of detection algorithms may be evaluated as a function of $\mathrm{SNR} = S/\sigma_{\tilde{w}}^2$ and saturation Ω. To illustrate the impact of Ω on the energy fluctuations, Figure 11b shows plots of the pdf of $10\log_{10}(P)$ for $T = 1$ sample (so coherent and incoherent are identical), $S = 1$, and $\mathrm{SNR} = 1/\sigma_{\tilde{w}}^2 = 10^3 = 30$ dB. Note that a small deviation in the saturation from $\Omega = 0$ causes a significant spread in the distribution of P around the unscattered signal power, $S = 1$ (0 dB). This variation in P affects detection performance and limits the performance of classification algorithms that use P as a feature.

Figure 12 illustrates signal saturation effects on detection probabilities. In this example, the Neyman-Pearson detection criterion [103] with false-alarm probability of 0.01 was used. The noise is zero-mean Gaussian, as in Section 2.2. When $\Omega = 0$, the detection probability is nearly zero for SNR= 2 dB but quickly changes to one when the SNR increases by about 6 dB. When $\Omega = 1$, however, the transition is much more gradual: even at SNR= 15 dB, the detection probability is less than 0.9.

The impact of scattering on classification performance can be illustrated by comparing the fluctuations in the measured harmonic signature, $\mathbf{P} = [P(\omega_1), \ldots, P(\omega_L)]^T$, with the "true" signature, $\mathbf{S} = [S(\omega_1), \ldots, S(\omega_L)]^T$, that would be measured in the absence of scattering and additive noise. Figures 11c and 11d illustrate this variability in the harmonic signature as the range to the target increases. Figure 11c shows the "ideal" harmonic signature for this example (no scattering and no noise). Figure 11d shows ± one standard deviation error bars on the harmonics for ranges 5, 10, 20, 40, 80, 160 m under "mostly sunny" conditions, using (83). For ranges beyond 80 m, the harmonic components display significant variations, and rank ordering of the harmonic amplitudes would exhibit variations also. The higher frequency harmonics experience larger variations, as expected. Classification based on relative harmonic amplitudes may experience significant performance degradations at these ranges, particularly for sources that have similar harmonic signatures.

4 Concluding Remarks

Aeroacoustics has a demonstrated capability for sensor networking applications, providing a low bandwidth sensing modality that leads to relatively low cost nodes. In battery operated conditions, where long lifetime in the field is expected, the node power budget is dominated by the cost of the communications. Consequently, the interplay between the communications and distributed signal processing is critical. We seek optimal network performance while minimizing the communication overhead.

We have considered the impact of the propagation phenomena on our ability to detect, localize, track, and classify acoustic sources. The strengths and limitations of acoustic sensing become clear in this light. Detection ranges and localization accuracy may be reasonably predicted. The turbulent atmosphere introduces spatial coherence losses that impact the ability to exploit large baselines between nodes for increased localization accuracy. The induced statistical fluctuations in amplitude place limits on the ability to classify sources at longer ranges. Very good performance has been demonstrated in many experiments; the analysis and experiments described here and elsewhere bound the problem and its solution space.

Because it is passive, and depends on the current atmospheric conditions, acoustic sensing may be strongly degraded in some cases. Passive sensing with high performance in all conditions will very likely require multiple sensing modalities, as well as hierarchical networks. This leads to interesting problems in fusion, sensor density and placement, as well as distributed processing and communications. For example, when very simple acoustic nodes with the limited capability of measuring loudness are densely deployed, they provide inherent localization capability [104, 105]. Such a system, operating at relatively short ranges, provides significant robustness to many of the limitations described here, and may act to queue other sensing modalities for classification or even identification.

Localization based on accurate angle of arrival estimation with short baseline arrays has been carefully analyzed, leading to well known triangulation strategies. Much more accurate localization, based on cooperative nodes, is possible in some conditions. These conditions depend fundamentally on the time-bandwidth of the observed signal, as well as the spatial coherence. For moving harmonic sources, these conditions are not likely to be supported, whereas sources that are more continuously broadband may be handled in at least some cases. It is important to note that the spatial coherence over a long baseline may be passively estimated in a straightforward way, leading to adaptive approaches that exploit the coherence when it is present. Localization updates, coupled with tracking, leads to an accurate picture of the nonstationary source environment.

Acoustic-based classification is the most challenging signal processing task, due to the source nonstationarities, inherent similarities between the sources, and propagation-induced statistical fluctuations. While the propagation places range limitations on present algorithms, it appears that the source similarities and nonstationarities may be the ultimate limiting factors in acoustic classification. Highly accurate classification will likely require the incorporation of other sensing modalities because of the challenging source characteristics.

Other interesting signal acoustic signal processing includes exploitation of Doppler, hierarchical and multi-modal processing, and handling multipath effects. Complex environments, such as indoor, urban, and forest, create multipath and diffraction that greatly complicate sensor signal processing and performance modeling. Improved understanding of the impact of these effects, and robust techniques for overcoming them, are needed. Exploitation of the very long range propagation distances possible with infrasound (frequencies below 20 Hz) [106] also requires further study and experimentation. Finally, we note that strong linkages between the communications network and the sensor signal processing are very important for overall resource utilization, especially including the multi-access protocol (MAC) networking layer.

Acknowledgment: The authors thank Tien Pham of the Army Research Laboratory for contributions to the wideband AOA estimation material in this chapter, and we thank Sandra Collier of the Army Research Laboratory for many helpful discussions on beamforming in random media.

References

[1] M. V. Namorato, "A concise history of acoustics in warfare," *Appl. Acoust.*, vol. 59, pp. 101-135, 2000.

[2] G. Becker and A. Güdesen, "Passive sensing with acoustics on the battlefield," *Appl. Acoust.*, vol. 59, pp. 149-178, 2000.

[3] N. Srour and J. Robertson, "Remote netted acoustic detection system," Army Research Laboratory Technical Report, ARL-TR-706, May 1995.

[4] T. F. W. Embleton, "Tutorial on sound propagation outdoors," *J. Acoust. Soc. Am.*, vol. 100, pp. 31–48, 1996.

[5] V. I. Tatarskii, *The Effects of the Turbulent Atmosphere on Wave Propagation* (Keter, Jerusalem, 1971).

[6] J. M. Noble, H. E. Bass, and R. Raspet, "The effect of large-scale atmospheric inhomogeneities on acoustic propagation," *J. Acoust. Soc. Am.*, vol. 92, pp. 1040–1046, 1992.

[7] D. K. Wilson and D. W. Thomson, "Acoustic propagation through anisotropic, surface-layer turbulence," *J. Acoust. Soc. Am.*, vol. 96, pp. 1080–1095, 1994.

[8] D.E. Norris, D.K. Wilson, D.W. Thomson, "Correlations between acoustic travel-time fluctuations and turbulence in the atmospheric surface layer," *Acta Acustica*, vol. 87, pp. 677–684, 2001.

[9] G. A. Daigle, T. F. W. Embleton, and J. E. Piercy, "Propagation of sound in the presence of gradients and turbulence near the ground," *J. Acoust. Soc. Am.*, vol. 79, pp. 613–627, 1986.

[10] V. E. Ostashev, *Acoustics in Moving Inhomogeneous Media* (E & FN Spon, London, 1997).

[11] D.K. Wilson, "A turbulence spectral model for sound propagation in the atmosphere that incorporates shear and buoyancy forcings", *J. Acoust. Soc. Am.*, **108** (5), Pt. 1, pp. 2021–2038, Nov. 2000.

[12] S.M. Kay, V. Nagesha, J. Salisbury, "Broad-band detection based on two-dimensional mixed autoregressive models," *IEEE Trans. on Signal Processing*, vol. 41, no. 7, pp. 2413–2428, July 1993.

[13] M. Agrawal and S. Prasad, "DOA estimation of wideband sources using a harmonic source model and uniform linear array," *IEEE Trans. on Signal Processing*, vol. 47, no. 3, pp. 619–629, March 1999.

[14] M. Feder, "Parameter estimation and extraction of helicopter signals observed with a wideband interference," *IEEE Trans. on Signal Processing*, vol. 41, no. 1, pp. 232–244, Jan. 1993.

[15] M. Zeytinoglu and K.M. Wong, "Detection of harmonic sets," *IEEE Trans. on Signal Processing*, vol. 43, no. 11, pp. 2618–2630, Nov. 1995.

[16] R.J. Kozick and B.M. Sadler, "Source Localization with Distributed Sensor Arrays and Partial Spatial Coherence," to appear in *IEEE Trans. on Signal Processing*, 2003.

[17] S. Morgan and R. Raspet, "Investigation of the mechanisms of low-frequency wind noise generation outdoors," *J. Acoust. Soc. Am.*, vol. 92, pp. 1180–1183, 1992.

[18] H.E. Bass, R. Raspet, and J.O. Messer, "Experimental determination of wind speed and direction using a three microphone array," *J. Acoust. Soc. Am.*, Vol. 97, pp. 695–696, 1995.

[19] E. M. Salomons, *Computational Atmospheric Acoustics* (Kluwer, Dordrecht, 2001).

[20] S. M. Kay, *Fundamentals of Statistical Signal Processing, Estimation Theory* (Prentice-Hall, 1993).

[21] D.K. Wilson, "Performance bounds for acoustic direction-of-arrival arrays operating in atmospheric turbulence," *J. Acoust. Soc. Am.*, vol. 103, no. 3, pp. 1306-1319, March 1998.

[22] S.L Collier and D.K. Wilson, "Performance bounds for passive arrays operating in a turbulent medium: Plane-wave analysis," *J. Acoust. Soc. Am.*, Vol. 113, No. 5, pp. 2704–2718, May 2003.

[23] S.L Collier and D.K. Wilson, "Performance bounds for passive sensor arrays operating in a turbulent medium II: Spherical-wave analysis," in review at *J. Acoust. Soc. Am.*, June 2003.

[24] V. E. Ostashev and D. K. Wilson, "Relative contributions from temperature and wind velocity fluctuations to the statistical moments of a sound field in a turbulent atmosphere," *Acta Acustica*, vol. 86, pp. 260–268, 2000.

[25] D.K. Wilson, B.M. Sadler, T. Pham, "Simulation of detection and beamforming with acoustical ground sensors," *Proc. SPIE 2002 AeroSense Symp.*, pp. 50–61, Orlando, FL, April 1-5, 2002.

[26] D. E. Norris, D. K. Wilson, and D. W. Thomson, "Atmospheric scattering for varying degrees of saturation and turbulent intermittency," *J. Acoust. Soc. Am.*, vol. 109, pp. 1871–1880, 2001.

[27] S. M. Flatté, R. Dashen, W. H. Munk, K. M. Watson, and F. Zachariasen, *Sound Transmission Through a Fluctuating Ocean* (Cambridge U. P., Cambridge, England, 1979).

[28] G. A. Daigle, J. E. Piercy, and T. F. W. Embleton, "Line-of-sight propagation through atmospheric turbulence near the ground," *J. Acoust. Soc. Am.*, vol. 74, pp. 1505–1513, 1983.

[29] H. E. Bass, L. N. Bolen, R. Raspet, W. McBride, and J. Noble, "Acoustic propagation through a turbulent atmosphere: experimental characterization," *J. Acoust. Soc. Am.*, vol. 90, pp. 3307–3313, 1991.

[30] A. Ishimaru, *Wave Propagation and Scattering in Random Media* (IEEE Press, New York, 1997).

[31] D.I. Havelock, M.R. Stinson, G.A. Daigle, "Measurements of the two-frequency mutual coherence function for sound propagation through a turbulent atmosphere," *J. Acoust. Soc. Am.*, **104** (1), pp. 91–99, July 1998.

[32] A. Paulraj and T. Kailath, "Direction of arrival estimation by eigenstructure methods with imperfect spatial coherence of wavefronts," *J. Acoust. Soc. Am.*, vol. 83, pp. 1034-1040, March 1988.

[33] B.-G. Song and J.A. Ritcey, "Angle of arrival estimation of plane waves propagating in random media," *J. Acoust. Soc. Am.*, vol. 99, no. 3, pp. 1370-1379, March 1996.

[34] A.B. Gershman, C.F. Mecklenbrauker, J.F. Bohme, "Matrix fitting approach to direction of arrival estimation with imperfect spatial coherence," *IEEE Trans. on Signal Proc.*, vol. 45, no. 7, pp. 1894-1899, July 1997.

[35] O. Besson, F. Vincent, P. Stoica, and A.B. Gershman, "Approximate maximum likelihood estimators for array processing in multiplicative noise environments," *IEEE Trans. on Signal Processing*, vol. 48, no. 9, pp. 2506 -2518, Sept. 2000.

[36] J. Ringelstein, A.B. Gershman, and J.F. Bohme, "Direction finding in random inhomogeneous media in the presence of multiplicative noise," *IEEE Signal Processing Letters*, vol. 7, no. 10, pp. 269–272, Oct. 2000.

[37] P. Stoica, O. Besson, A.B. Gershman, "Direction-of-arrival estimation of an amplitude-distorted wavefront," *IEEE Trans. on Signal Processing*, vol. 49, no. 2, pp. 269–276, Feb. 2001.

[38] O. Besson, P. Stoica, A.B. Gershman, "Simple and accurate direction of arrival estimator in the case of imperfect spatial coherence," *IEEE Trans. on Signal Processing*, vol. 49, no. 4, pp. 730–737, April 2001.

[39] M. Ghogho, O. Besson, and A. Swami, "Estimation of directions of arrival of multiple scattered sources," *IEEE Trans. on Signal Processing*, vol. 49, no. 11, pp. 2467–2480, Nov. 2001.

[40] G. Fuks, J. Goldberg, H. Messer, "Bearing estimation in a Ricean channel–Part I: Inherent accuracy limitations," *IEEE Trans. on Signal Processing*, vol. 49, no. 5, pp. 925–937, May 2001.

[41] J. F. Boehme, "Array processing," chapter 1 in *Advances in Spectrum Analysis and Array Processing, Vol. 2,* S. Haykin, ed. (Prentice-Hall, 1991).

[42] H. L. Van Trees, *Optimum Array Processing* (Wiley, 2002).

[43] N. Owsley, "Sonar array processing," in *Array Signal Processing,* S. Haykin ed. (Prentice-Hall, 1984).

[44] G. Su, M. Morf "Signal subspace approach for multiple wideband emitter location," *IEEE Trans. ASSP,* Vol. 31, no. 6, pp. 1502–1522, December 1983.

[45] H. Wang and M. Kaveh, "Coherent signal-subspace processing for the detection and estimation of angles of arrival of multiple wide-band sources," *IEEE Trans. ASSP,* volȦSSP-33, no. 4, pp. 823–831, August 1985.

[46] D. N. Swingler and J. Krolik, "Source location bias in the coherently focused high-resolution broad-band beamformer," *IEEE Trans. ASSP,* Vol. 37, No. 1, pp. 143–145, January 1989.

[47] S. Valaee and P. Kabal, "Wideband array processing using a two-sided correlation transformation," *IEEE Trans. SP,* Vol. 43, No. 1, pp. 160–172, January 1995.

[48] J. Krolik and D. Swingler, "Focused wide-band array processing by spatial resampling," *IEEE Trans. ASSP,* Vol. 38, No. 2, pp. 356–360, February 1990.

[49] J. Krolik, "Focused wide-band array processing for spatial spectral estimation," chapter 6 in *Advances in Spectrum Analysis and Array Processing, Vol. 2,* S. Haykin, ed. (Prentice-Hall, 1991).

[50] B. Friedlander, A. J. Weiss, "Direction finding for wide-band signals using an interpolated array," *IEEE Trans. SP,* Vol. 41, No. 4, pp. 1618–1634, April 1993.

[51] M. A. Doron, E. Doron, and A. J. Weiss, "Coherent wide-band processing for arbitrary array geometry," *IEEE Trans. SP,* Vol. 41, No. 1, pp. 414–417, January 1993.

[52] K. M. Buckley and L. J. Griffiths, "Broad-band signal-subspace spatial-spectrum (BASS-ALE) estimation," *IEEE Trans. ASSP,* Vol. 36, No. 7, pp. 953–964, July 1988.

[53] M. Agrawal, S. Prasad, "Broadband DOA estimation using spatial-only modeling of array data," *IEEE Trans. SP,* Vol. 48, No. 3, pp. 663–670, March 2000.

[54] S. Sivanand, J. Yang, and M. Kaveh, "Focusing filters for wide-band direction finding," *IEEE Trans. SP,* Vol. 39, No. 2, pp. 437–445, February 1991.

[55] S. Sivanand and M. Kaveh, "Multichannel filtering for wide-band direction finding," *IEEE Trans. SP,* Vol. 39, No. 9, pp. 2128–2132, September 1991.

[56] S. Sivanand, "On focusing preprocessor for broadband beamforming," *Sixth SP Workshop on Stat. Sig. and Array Proc.,* pp. 350–353, Victoria, BC, Canada, October 1992.

[57] D. B. Ward, Z. Ding, R. A Kennedy, "Broadband DOA estimation using frequency invariant beamforming," *IEEE Trans. SP,* Vol. 46, No. 5, pp. 1463–1469, May 1998.

[58] W. J. Bangs, "Array processing with generalized beamformers," PhD Dissertation, Yale University, 1972.

[59] D. N. Swingler, "An approximate expression for the Cramer-Rao bound on DOA estimates of closely spaced sources in broadband line-array beamforming," *IEEE Trans. SP,* Vol. 42, No. 6, pp. 1540–1543, June 1994.

[60] J. Yang and M. Kaveh, "Coherent signal-subspace transformation beamformer," *IEE Proc.,* Vol. 137, Pt. F, No. 4, pp. 267–275, August 1990.

[61] T. Pham and B. M. Sadler, "Acoustic tracking of ground vehicles using ESPRIT", *SPIE Proc. Volume 2485,* Automatic Object Recognition V, Orlando FL, April 1995, pp. 268–274.

[62] T. Pham and B. M. Sadler, M. Fong, and D. Messer, "High resolution acoustic direction finding algorithm to detect and track ground vehicles," *20th Army Science Conference,* Norfolk, VA, June 1996; see also *Twentieth Army Science Conference, Award Winning Papers* (World Scientific, 1997).

[63] T. Pham and B. M. Sadler, "Adaptive wideband aeroacoustic array processing," *8th IEEE Statistical Signal and Array Processing Workshop,* pp. 295–298, Corfu, Greece, June 1996.

[64] T. Pham and B. M. Sadler, "Adaptive wideband aeroacoustic array processing," *Proceedings of the 1st Annual Conference of the Sensors and Electron Devices Federated Laboratory Research Program,* College Park, MD, January 1997.

[65] T. Pham, B. M. Sadler, "Focused wideband array processing algorithms for high-resolution direction finding," *Proc. MSS Specialty Group on Acoustics and Seismic Sensing,* September 1998.

[66] T. Pham, B. M. Sadler, "Wideband array processing algorithms for acoustic tracking of ground vehicles," *Proc. 21st Army Science Conference,* 1998.

[67] R.R. Tenney and J.R. Delaney, "A distributed aeroacoustic tracking algorithm," *Proc. American Control Conf.*, pp. 1440-1450, June 1984.

[68] Y. Bar-Shalom and X.-R. Li, *Multitarget-Multisensor Tracking: Principles and Techniques*, YBS, 1995.

[69] A. Farina, "Target tracking with bearings-only measurements," *Signal Processing*, vol. 78, pp. 61-78, 1999.

[70] B. Ristic, S. Arulampalam, C. Musso, "The influence of communication bandwidth on target tracking with angle only measurements from two platforms," *Signal Processing*, vol. 81, pp. 1801-1811, 2001.

[71] L.M. Kaplan, P. Molnar, Q. Le, "Bearings-only target localization for an acoustical unattended ground sensor network," *Proc. SPIE AeroSense*, Orlando, Florida, April 2001.

[72] A.J. Weiss and E. Weinstein, "Fundamental limitations in passive time delay estimation - part 1: narrowband systems," *IEEE Trans. Acoust., Speech, Sig. Proc.*, vol. ASSP-31, no. 2, pp. 472-485, April 1983.

[73] E. Weinstein and A.J. Weiss, "Fundamental limitations in passive time delay estimation - part 2: wideband systems," *IEEE Trans. Acoust., Speech, Sig. Proc.*, vol. ASSP-32, no. 5, pp. 1064–1077, Oct. 1984.

[74] K. Bell, "Wideband direction of arrival (DOA) estimation for multiple aeroacoustic sources," *Proc. 2000 Meeting of the MSS Specialty Group on Battlefield Acoustics and Seismics*, Laurel, MD, October 18-20, 2000.

[75] K. Bell, "Maximum a posteriori (MAP) multitarget tracking for broadband aeroacoustic sources," *Proc. 2001 Meeting of the MSS Specialty Group on Battlefield Acoustics and Seismics*, Laurel, MD, October 23–26, 2001.

[76] M. Wax and T. Kailath, "Decentralized processing in sensor arrays," *IEEE Trans. on Acoustics, Speech, Signal Processing*, vol. ASSP-33, no. 4, pp. 1123-1129, October 1985.

[77] P. Stoica, A. Nehorai, and T. Soderstrom, "Decentralized array processing using the MODE algorithm," *Circuits, Systems, and Signal Processing*, vol. 14, no. 1, 1995, pp. 17-38.

[78] E. Weinstein, "Decentralization of the Gaussian maximum likelihood estimator and its applications to passive array processing," *IEEE Trans. Acoust., Speech, Sig. Proc.*, vol. ASSP-29, no. 5, pp. 945-951, October 1981.

[79] R.L. Moses and R. Patterson, "Self-calibration of sensor networks," *Proc. SPIE AeroSense 2002*, Vol. 4743 (2002), pp. 108–119, April 2002.

[80] J. L. Spiesberger, "Locating animals from their sounds and tomography of the atmosphere: Experimental demonstration," *J. Acoust. Soc. Am.*, vol. 106, pp. 837–846 (1999).

[81] D. K. Wilson, A. Ziemann, V. E. Ostashev, and A. G. Voronovich, "An overview of acoustic travel-time tomography in the atmosphere and its potential applications," *Acta Acustica*, vol. 87, pp. 721–730, 2001.

[82] B.G. Ferguson, "Variability in the passive ranging of acoustic sources in air using a wavefront curvature technique," *J. Acoust. Soc. Am.*, vol. 108, no. 4, pp. 1535-1544, Oct. 2000.

[83] B.G. Ferguson, "Time-delay estimation techniques applied to the acoustic detection of jet aircraft transits," *J. Acoust. Soc. Am.*, vol. 106, no. 1, pp. 255-264, July 1999.

[84] B. Friedlander, "On the Cramer-Rao Bound for Time Delay and Doppler Estimation," *IEEE Trans. on Info. Theory*, vol. IT-30, no. 3, pp. 575-580, May 1984.

[85] P. Whittle, "The analysis of multiple stationary time series," *J. Royal Statist. Soc.*, vol. 15, pp. 125-139, 1953.

[86] G.C. Carter (ed.), *Coherence and Time Delay Estimation* (Selected Reprint Volume), IEEE Press, 1993.

[87] C.H. Knapp and G.C. Carter, “Estimation of time delay in the presence of source or receiver motion,” *J. Acoust. Soc. Am.*, vol. 61, no. 6, pp. 1545-1549, June 1977.

[88] W.B. Adams, J.P. Kuhn, W.P. Whyland, “Correlator compensation requirements for passive time-delay estimation with moving source or receivers,” *IEEE Trans. Acoust., Speech, Signal Processing*, vol. ASSP-28, no. 2, pp. 158-168, April 1980.

[89] R.J. Kozick and B.M. Sadler, “Tracking Moving Acoustic Sources with a Network of Sensors,” Army Research Laboratory Technical Report ARL-TR-2750, October 2002.

[90] V. Katkovnik and A.B. Gershman, “A local polynomial approximation based beamforming for source localization and tracking in nonstationary environments,” *IEEE Signal Processing Letters*, vol. 7, no. 1, pp. 3-5, Jan. 2000.

[91] J.W. Betz, “Comparison of the deskewed short-time correlator and the maximum likelihood correlator,” *IEEE Trans. Acoust., Speech, Signal Processing*, vol. ASSP-32, no. 2, pp. 285-294, April 1984.

[92] P.M. Schultheiss and E. Weinstein, “Estimation of differential Doppler shifts,” *J. Acoust. Soc. Am.*, vol. 66, no. 5, pp. 1412-1419, Nov. 1979.

[93] R.J. Kozick and B.M. Sadler, “Information Sharing Between Localization, Tracking, and Identification Algorithms,” *Proc. 2002 Meeting of the MSS Specialty Group on Battlefield Acoustics and Seismics*, Laurel, MD, Sept. 24–27, 2002.

[94] T.R. Damarla, T. Pham, J. Gerber, D. Hillis, “Army acoustic tracking algorithm,” *Proc. 2002 Meeting of the MSS Specialty Group on Battlefield Acoustics and Seismics*, Laurel, MD, Sept. 24–27, 2002.

[95] M. Wellman, N. Srour, and D.B. Hillis, “Acoustic feature extraction for a neural network classifier,” Army Research Laboratory, ARL-TR-1166, Jan. 1997.

[96] N. Srour, D. Lake, and M. Miller, “Utilizing acoustic propagation models for robust battlefield target identification,” *Proc. 1998 Meeting of the IRIS Specialty Group on Acoustic and Seismic Sensing*, Sept. 1998.

[97] D. Lake, “Robust battlefield acoustic target identification,” *Proc. 1998 Meeting of the IRIS Specialty Group on Acoustic and Seismic Sensing*, Sept. 1998.

[98] D. Lake, “Efficient maximum likelihood estimation for multiple and coupled harmonics,” Army Research Laboratory, ARL-TR-2014, Dec. 1999.

[99] D. Lake, “Harmonic phase coupling for battlefield acoustic target identification,” *Proc. IEEE ICASSP*, pp. 2049–2052, 1998.

[100] H. Hurd and T.Pham, “Target association using harmonic frequency tracks,” *Proc. Fifth IEEE Int. Conf. on Information Fusion*, pp. 860–864, 2002.

[101] H. Wu and J.M. Mendel, “Data analysis and feature extraction for ground vehicle identification using acoustic data,” *2001 MSS Specialty Group Meeting on Battlefield Acoustics and Seismic Sensing*, Johns Hopkins University, Laurel, MD, Oct. 2001.

[102] H. Wu and J.M. Mendel, “Classification of ground vehicles from acoustic data using fuzzy logic rule-based classifiers: early results,” *Proc. SPIE AeroSense*, pp. 62–72, Orland, FL, April 1–5, 2002.

[103] S. M. Kay, *Fundamentals of Statistical Signal Processing, Detection Theory* (Prentice-Hall, 1998).

[104] T. Pham, B. M. Sadler, “Energy-based detection and localization of stochastic signals,” *2002 Meeting of the MSS Specialty Group on Battlefield Acoustic and Seismic Sensing*, Laurel, MD September 2002.

[105] T. Pham, “Localization algorithms for ad-hoc network of disposable sensors,” *2003 MSS National Symposium on Sensor and Data Fusion*, San Diego, CA, June 2003.

[106] A.J. Bedard and T.M. Georges, “Atmospheric infrasound,” *Physics Today*, vol. 53, pp. 32–37 (2000).

Table and Figure Captions

Table 1: Modeled turbulence quantities and inverse extinction coefficients for various atmospheric conditions. The atmospheric conditions are described quantitatively in [24]. The second and third columns give the inverse extinction coefficients at 50 Hz and 200 Hz, respectively. These values indicate the distance at which random fluctuations in the complex signal become strong. The fourth and fifth columns represent the relative contributions of temperature and wind fluctuations to the field coherence. The sixth column is the effective integral length scale for the scattered sound field; at sensor separations greater than this value, the coherence is "saturated."

Figure 1: Geometry of source and sensor locations.

Figure 2: Processing to obtain in-phase and quadrature components, $z^{(\mathrm{I})}(t)$ and $z^{(\mathrm{Q})}(t)$.

Figure 3: Turbulence-induced distortions of acoustic wavefronts impinging on an array. The wavefronts are initially smooth (left) and become progressively more distorted until they arrive at the array (right). Top: Sensor separations within the inertial subrange of the turbulence ($\rho \gg \ell$ and $\rho \ll \mathcal{L}$). The wavefronts are fairly smooth but the AOA (and therefore the apparent source bearing) varies. Bottom: Sensor separations much larger than the scale of the largest turbulent eddies ($\rho \gg \mathcal{L}$). The wavefronts have a very rough appearance and the effect of the scattering is similar to uncorrelated noise.

Figure 4: Left: Characteristic behavior of the second-moment extinction coefficient, $\nu(\rho)$. It initially increases with increasing sensor separation ρ, and then saturates at a fixed value 2μ (where μ is the first-moment extinction coefficient) when ρ is large compared to the size of the largest turbulent eddies. Right: Resulting behavior of the total signal coherence, B_{mn}, (42), for several values of the propagation distance d_o.

Figure 5: Evaluation of the coherence of the scattered signals at sensors with separation ρ, using $f = 50$ Hz, $d_o = 1,500$ m, mostly sunny, light wind conditions (Table 1), $\nu(\rho)$ is computed with (54), and the coherence, $\gamma(\rho)$, is computed with (40).

Figure 6: Experimental wideband AOA estimation over 250 seconds, covering a range of approximately ±1 kilometers. Three methods are depicted with M highest SNR frequency bins: (a) narrowband MUSIC ($M = 1$), (b) incoherent MUSIC ($M = 20$), and (c) CSM-MUSIC ($M = 20$). Solid lines depict GPS-derived AOA ground truth.

Figure 7: Geometry of non-moving source location and an array of arrays. A communication link is available between each array and the fusion center.
(Originally published in [16], ©2003 IEEE, reprinted with permission.)

Figure 8: RMS source localization error ellipses based on the CRB for $H = 3$ arrays and one *narrowband* source in (a)-(c) and one *wideband* source in (d)-(f).
(Originally published in [16], ©2003 IEEE, reprinted with permission.)

Figure 9: Threshold coherence versus bandwidth based on (80) for (a) $\omega_0 = 2\pi 50$ rad/sec, $\mathcal{T} = 2$ sec and (b) $\omega_0 = 2\pi 100$ rad/sec, $\mathcal{T} = 1$ sec for SNRs $G_s/G_w = 0, 10,$ and ∞ dB. (c) Threshold coherence value from (80) versus time-bandwidth product $\left(\frac{\Delta\omega\cdot\mathcal{T}}{2\pi}\right)$ for several values of fractional bandwidth $\left(\frac{\Delta\omega}{\omega_0}\right)$ and high SNR, $G_s/G_w \rightarrow \infty$.
(Originally published in [16], ©2003 IEEE, reprinted with permission.)

Figure 10: (a) Location of nodes. (b) PSDs at nodes 1 and 3 when transmitter is at node 0. (c) Coherence between nodes 1 and 3. (d) Intersection of hyperbolas obtained from differential time delays estimated at nodes 1, 2, and 3. (e) Expanded view of part (d).
(Originally published in [16], ©2003 IEEE, reprinted with permission.)

Figure 11: (a) Variation of saturation Ω with frequency f and range d_o. (b) Probability density function (pdf) of average power $10\log_{10}(P)$ measured at the sensor for $T = 1$ sample of a signal with $S = 1$ (0 dB), SNR $= 1/\sigma_{\tilde{w}}^2 = 10^3 = 30$ dB, and various values of the saturation, Ω. (c) Harmonic signature with no scattering. (d) Error bars for harmonic signatures ± one standard deviation caused by scattering at different source ranges.

Figure 12: Probability of detection as a function of SNR for several values of the saturation parameter Ω. The Neyman-Pearson criterion is used with probability of false-alarm $P_{\mathrm{FA}} = 0.01$.

Atmospheric condition	μ^{-1} (m) at 50 Hz	μ^{-1} (m) at 200 Hz	C_T^2/T_0^2 ($\mathrm{m}^{-2/3}$)	$(22/3)C_\upsilon^2/c_0^2$ ($\mathrm{m}^{-2/3}$)	$\mathcal{L}_{\mathrm{eff}}$ (m)
Mostly sunny, light wind	990	62	2.0×10^{-5}	8.0×10^{-6}	100
Mostly sunny, moderate wind	980	61	7.6×10^{-6}	2.8×10^{-5}	91
Mostly sunny, strong wind	950	59	2.4×10^{-6}	1.3×10^{-4}	55
Mostly cloudy, light wind	2900	180	1.5×10^{-6}	4.4×10^{-6}	110
Mostly cloudy, moderate wind	2800	180	4.5×10^{-7}	2.4×10^{-5}	75
Mostly cloudy, strong wind	2600	160	1.1×10^{-7}	1.2×10^{-4}	28

Table 1: Modeled turbulence quantities and inverse extinction coefficients for various atmospheric conditions. The atmospheric conditions are described quantitatively in [24]. The second and third columns give the inverse extinction coefficients at 50 Hz and 200 Hz, respectively. These values indicate the distance at which random fluctuations in the complex signal become strong. The fourth and fifth columns represent the relative contributions of temperature and wind fluctuations to the field coherence. The sixth column is the effective integral length scale for the scattered sound field; at sensor separations greater than this value, the coherence is “saturated.”

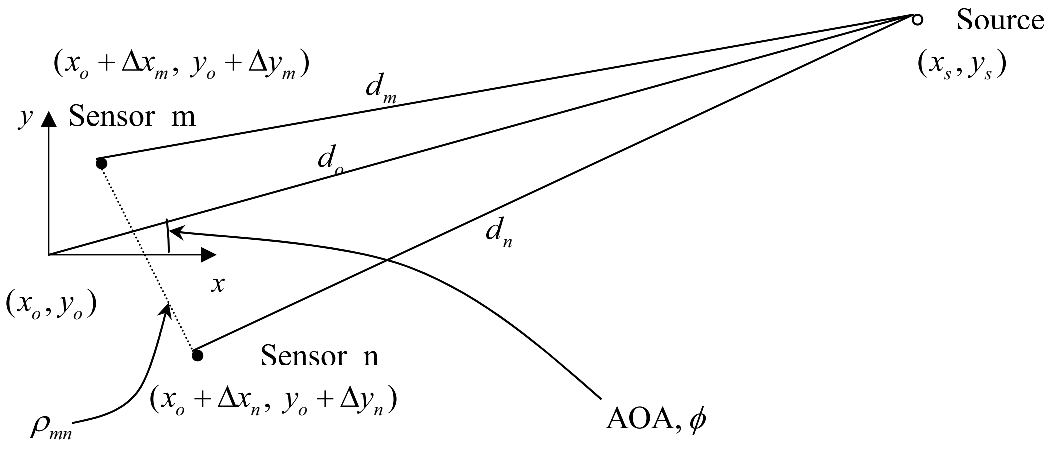

Figure 1: Geometry of source and sensor locations.

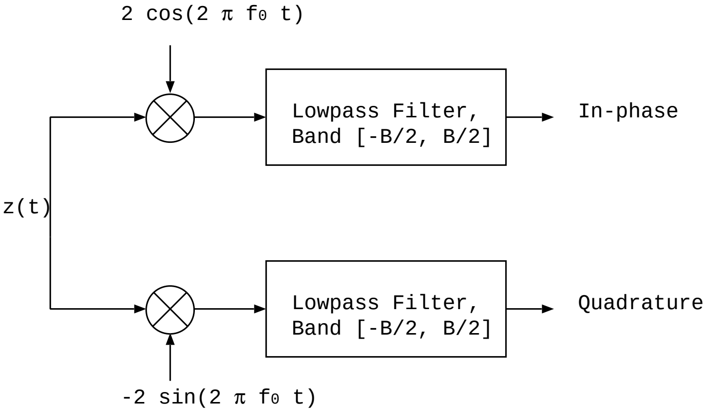

Figure 2: Processing to obtain in-phase and quadrature components, $z^{(\mathrm{I})}(t)$ and $z^{(\mathrm{Q})}(t)$.

** See files fig3.jpg, fig3.tif, or fig3.pdf, and the pictures on the next page **

Figure 3: Turbulence-induced distortions of acoustic wavefronts impinging on an array. The wavefronts are initially smooth (left) and become progressively more distorted until they arrive at the array (right). Top: Sensor separations within the inertial subrange of the turbulence ($\rho \gg \ell$ and $\rho \ll \mathcal{L}$). The wavefronts are fairly smooth but the AOA (and therefore the apparent source bearing) varies. Bottom: Sensor separations much larger than the scale of the largest turbulent eddies ($\rho \gg \mathcal{L}$). The wavefronts have a very rough appearance and the effect of the scattering is similar to uncorrelated noise.

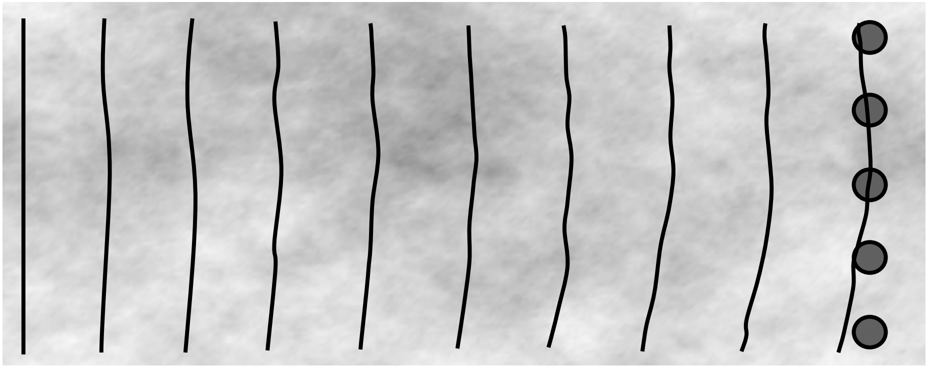

$\rho << L$

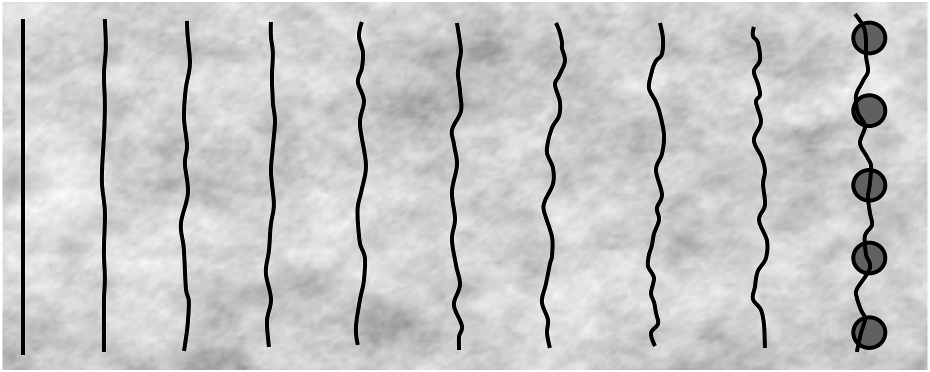

$\rho >> L$

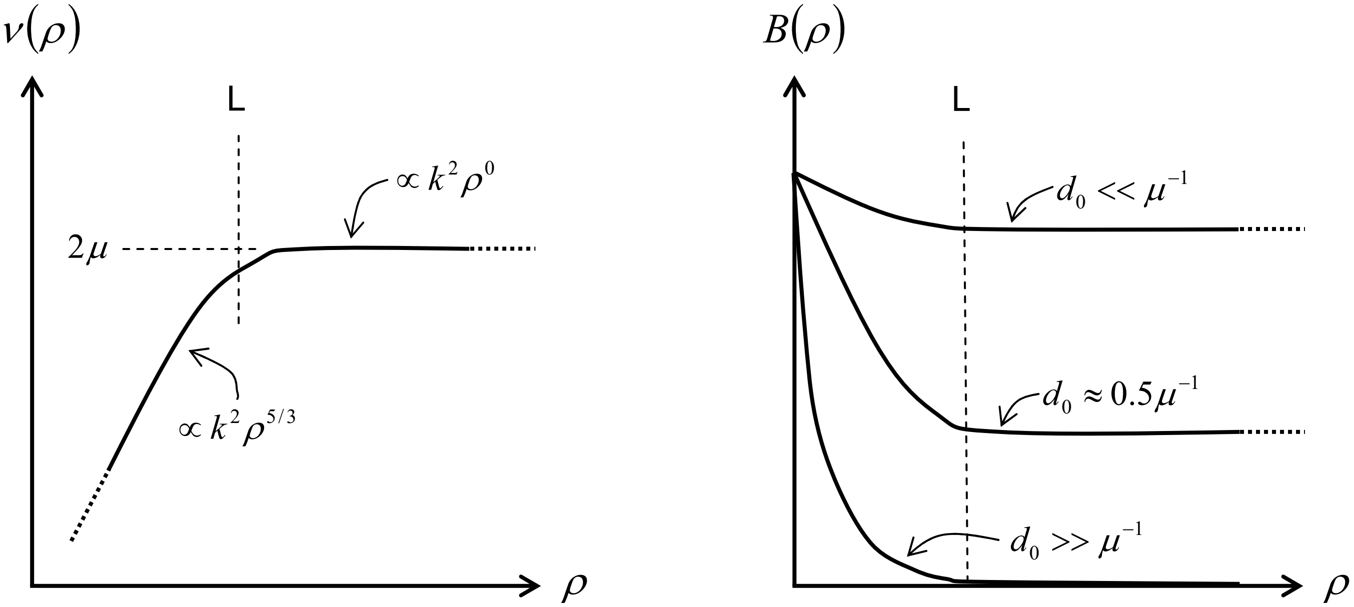

Figure 4: Left: Characteristic behavior of the second-moment extinction coefficient, $\nu(\rho)$. It initially increases with increasing sensor separation ρ, and then saturates at a fixed value 2μ (where μ is the first-moment extinction coefficient) when ρ is large compared to the size of the largest turbulent eddies. Right: Resulting behavior of the total signal coherence, B_{mn}, (42), for several values of the propagation distance d_o.

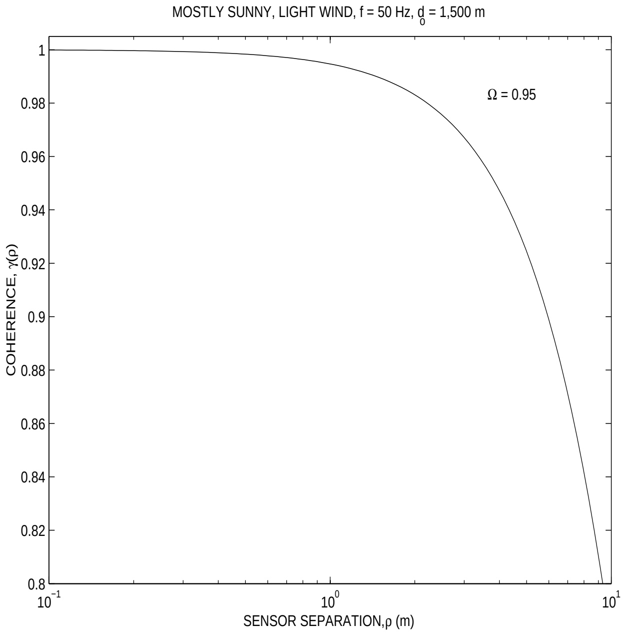

Figure 5: Evaluation of the coherence of the scattered signals at sensors with separation ρ, using $f = 50$ Hz, $d_o = 1,500$ m, mostly sunny, light wind conditions (Table 1), $\nu(\rho)$ is computed with (54), and the coherence, $\gamma(\rho)$, is computed with (40).

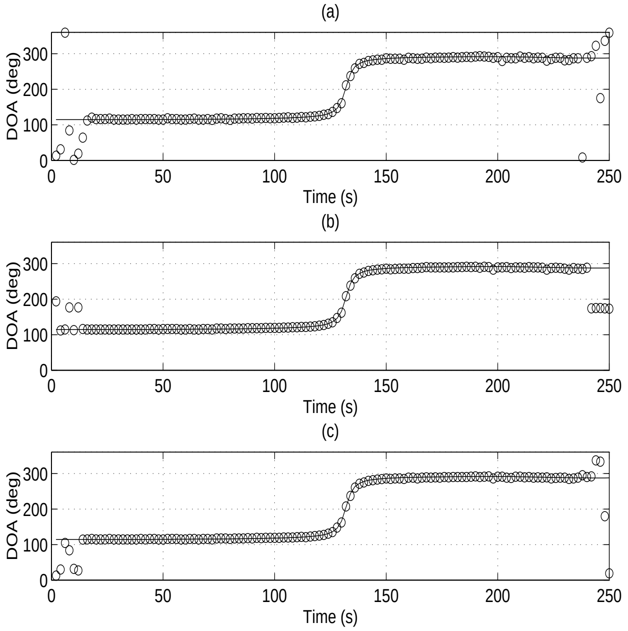

Figure 6: Experimental wideband AOA estimation over 250 seconds, covering a range of approximately ±1 kilometers. Three methods are depicted with M highest SNR frequency bins: (a) narrowband MUSIC ($M = 1$), (b) incoherent MUSIC ($M = 20$), and (c) CSM-MUSIC ($M = 20$). Solid lines depict GPS-derived AOA ground truth.

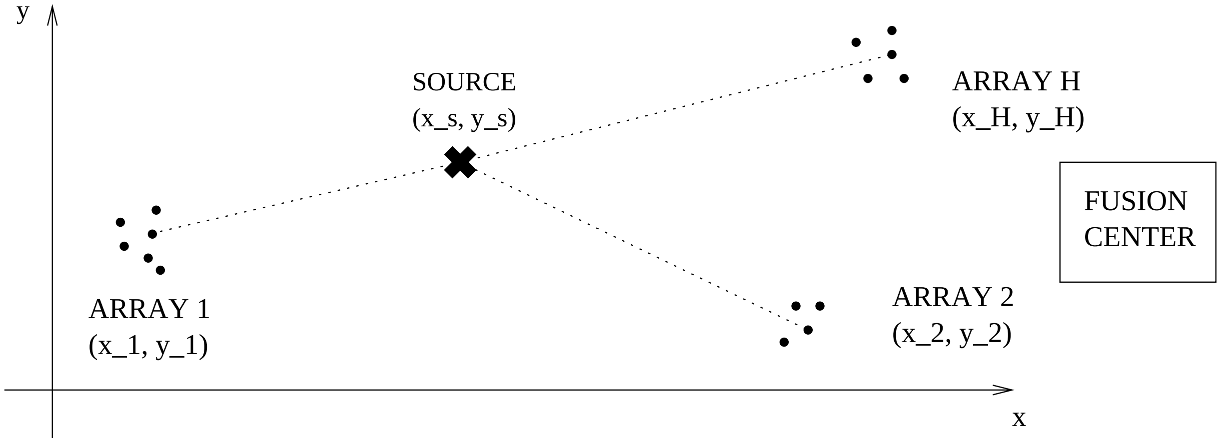

Figure 7: Geometry of non-moving source location and an array of arrays. A communication link is available between each array and the fusion center. (Originally published in [16], ©2003 IEEE, reprinted with permission.)

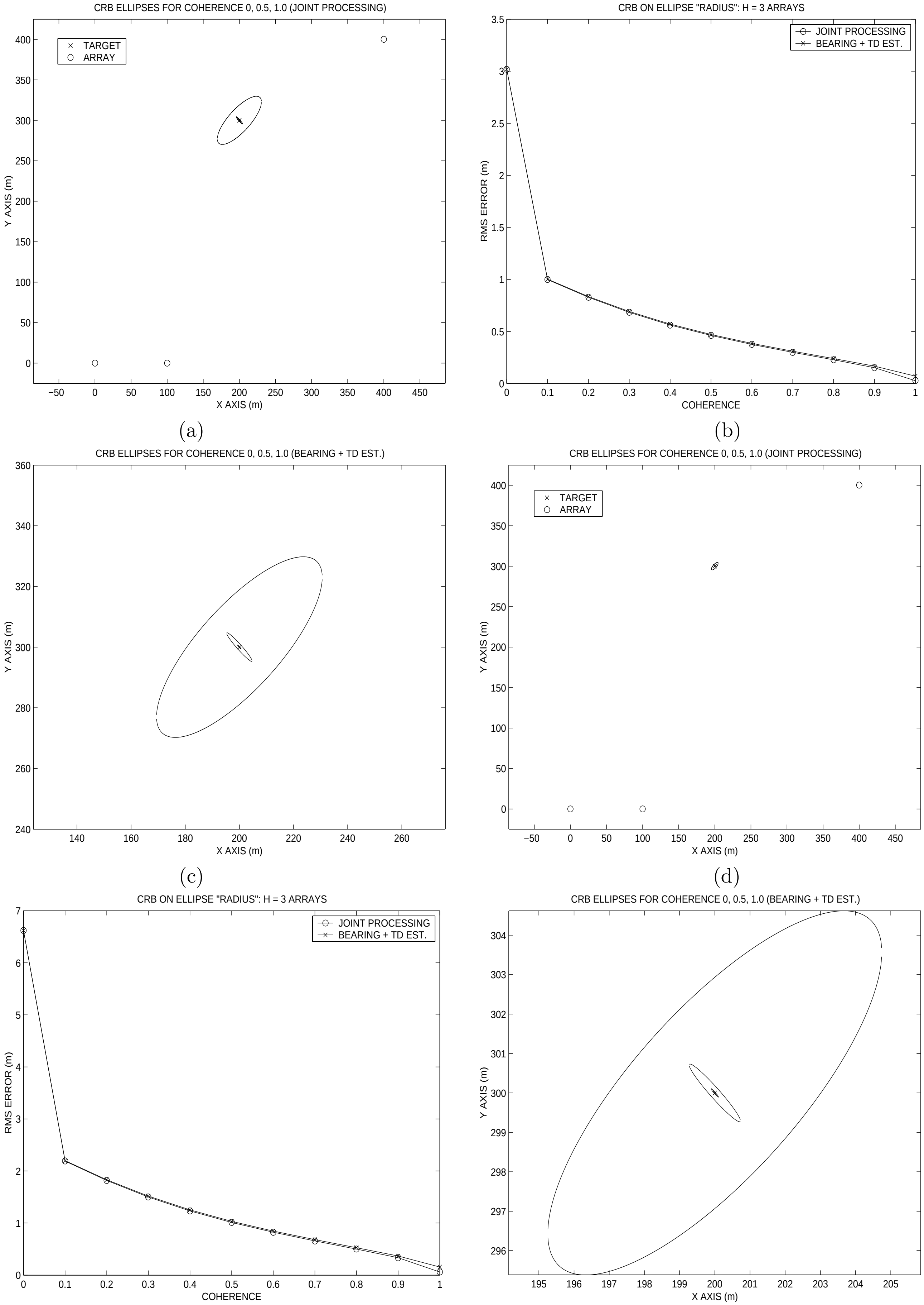

(a) (b)

(c) (d)

(e) (f)

Figure 8: RMS source localization error ellipses based on the CRB for $H = 3$ arrays and one *narrowband* source in (a)-(c) and one *wideband* source in (d)-(f). (Originally published in [16], ©2003 IEEE, reprinted with permission.)

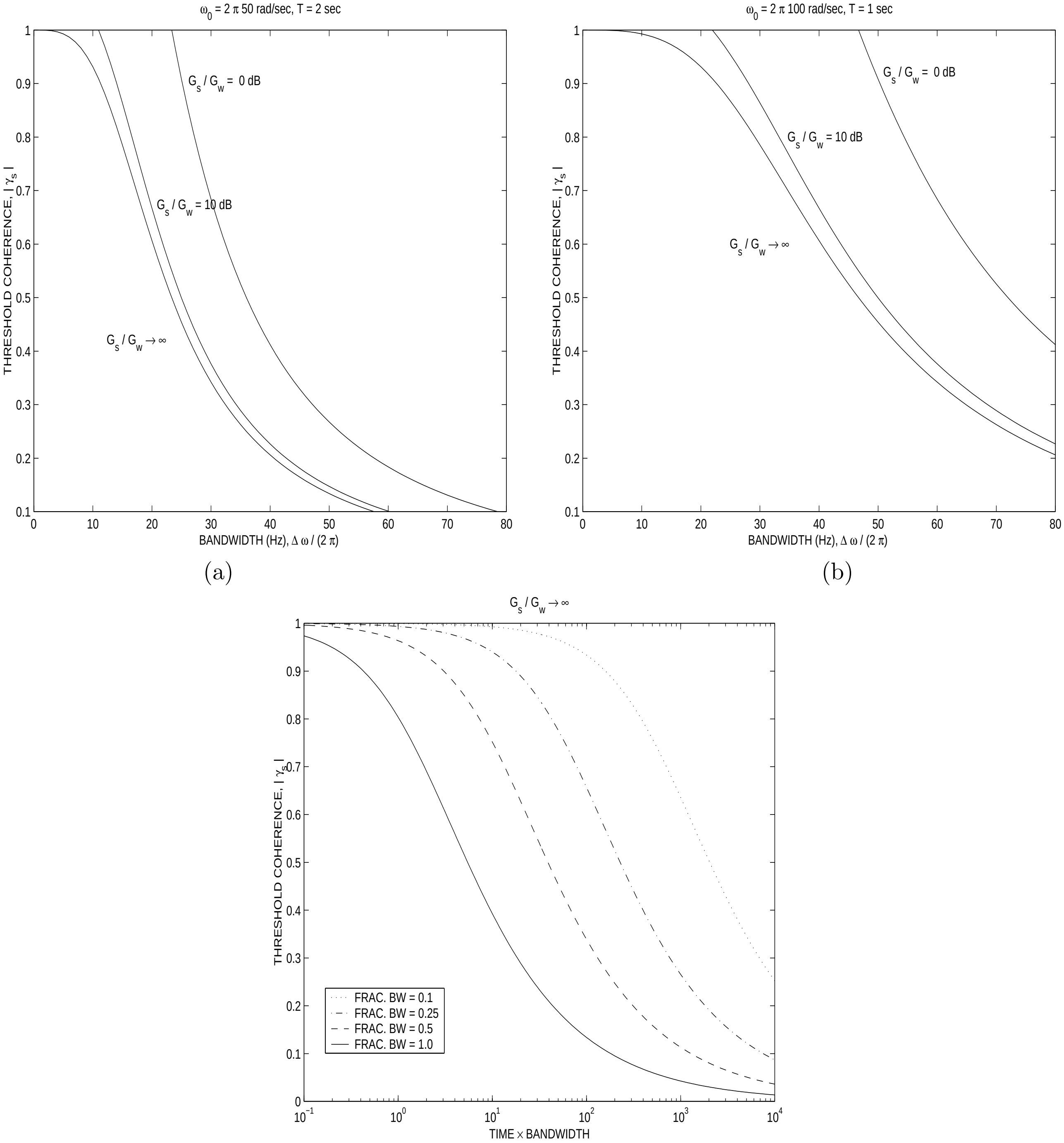

(a)

(b)

(c)

Figure 9: Threshold coherence versus bandwidth based on (80) for (a) $\omega_0 = 2\pi 50$ rad/sec, $\mathcal{T} = 2$ sec and (b) $\omega_0 = 2\pi 100$ rad/sec, $\mathcal{T} = 1$ sec for SNRs $G_s/G_w = 0, 10$, and ∞ dB. (c) Threshold coherence value from (80) versus time-bandwidth product $\left(\frac{\Delta\omega \cdot \mathcal{T}}{2\pi}\right)$ for several values of fractional bandwidth $\left(\frac{\Delta\omega}{\omega_0}\right)$ and high SNR, $G_s/G_w \to \infty$. (Originally published in [16], ©2003 IEEE, reprinted with permission.)

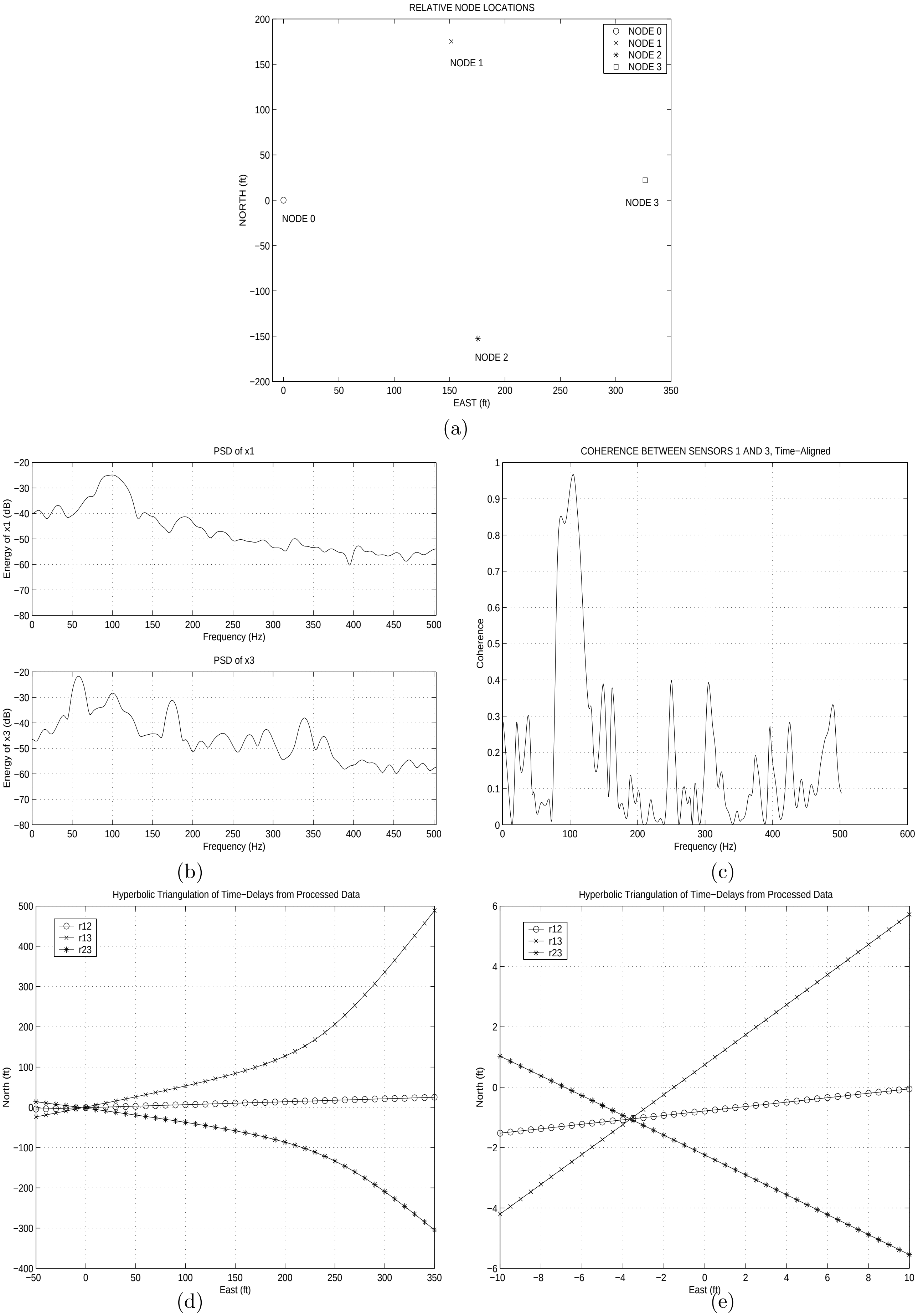

Figure 10: (a) Location of nodes. (b) PSDs at nodes 1 and 3 when transmitter is at node 0. (c) Coherence between nodes 1 and 3. (d) Intersection of hyperbolas obtained from differential time delays estimated at nodes 1, 2, and 3. (e) Expanded view of part (d). (Originally published in [16], ©2003 IEEE, reprinted with permission.)

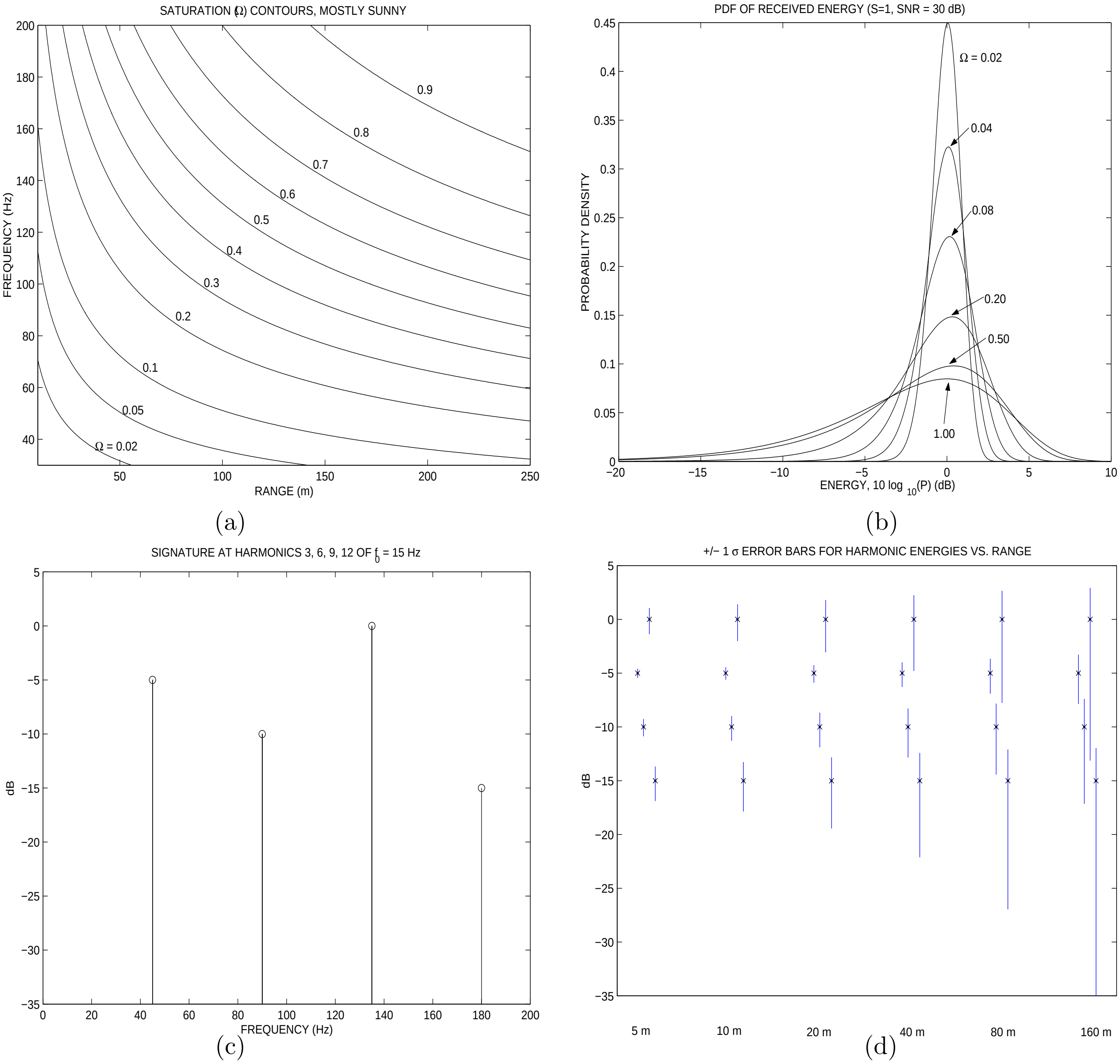

(a) (b) (c) (d)

Figure 11: (a) Variation of saturation Ω with frequency f and range d_o. (b) Probability density function (pdf) of average power $10\log_{10}(P)$ measured at the sensor for $T = 1$ sample of a signal with $S = 1$ (0 dB), $\mathrm{SNR} = 1/\sigma^2_{\tilde{w}} = 10^3 = 30$ dB, and various values of the saturation, Ω. (c) Harmonic signature with no scattering. (d) Error bars for harmonic signatures ± one standard deviation caused by scattering at different source ranges.

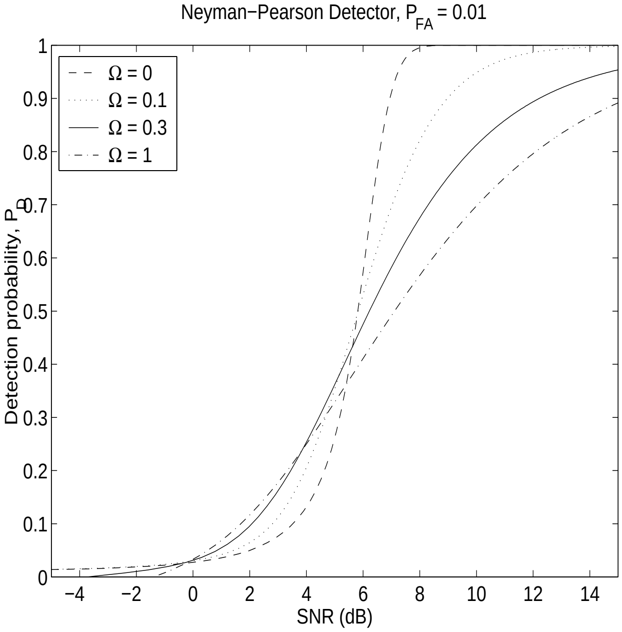

Figure 12: Probability of detection as a function of SNR for several values of the saturation parameter Ω. The Neyman-Pearson criterion is used with probability of false-alarm $P_{\text{FA}} = 0.01$.